RESEARCH ARTICLE

Contextual Regularization-Based Energy Optimization for Segmenting Breast Tumor in DCE-MRI

PRIYADHARSHINI BABU, MYTHILI ASAITHAMBI, (Member, IEEE), AND SUDHAKAR MOGAPPAIR SURIYAKUMAR

School of Electronics Engineering, Vellore Institute of Technology, Vellore, Tamil Nadu 632014, India

Corresponding author: Mythili Asaithambi (mythili.asaithambi@vit.ac.in)

ABSTRACT Accurate breast tumor segmentation is crucial for precise diagnosis, effective treatment planning, and the development of automated decision-support systems in clinical practice. The imprecision of trending segmentation models in differentiating tumors from their surrounding tissues, particularly in weighing the boundary pixels across tumor regions poses a significant challenge in precise tumor delineation. Dynamic contrast-enhanced magnetic resonance imaging (DCE-MRI) effectively captures tumor vascularity and perfusion dynamics and is a reliable modality for extracting the region of interest (ROI). Nevertheless, the intricate intensity variations in DCE-MRI owing to heterogeneous tumor morphology pose considerable challenges in tumor delineation, necessitating a highly adaptive and robust model for precise tumor segmentation. Accordingly, this manuscript presents a Contextual Regularization-Based Energy Optimization (CRBEO) model that effectively captures these intensity variations in the form of energies contributed by data fidelity and regularization terms. The formulated non-linear energy-based convex optimizer is adaptively tuned by a variational Minimax principle to achieve the desired solution. An iterative gradient descent algorithm is engaged to minimize the energy-based cost function, obtaining stable convergence towards the optimal solution. The extensive relative analysis of CRBEO on complex breast DCE-MRI datasets including QIN breast DCE-MRI, TCGA-BRCA, BreastDM, RIDER, and ISPY1 has recorded significant dice improvements of 30.16%, 11.48%, 20.66%, 1.012%, and 28.107%, respectively on par with trending SOTA methods. The complexity analysis of CRBEO with time and space has justified its extension to real-time clinical diagnosis.

INDEX TERMS Breast tumor segmentation, contextual regularization-based energy optimization (CRBEO), DCE-MRI, gradient optimization, Hessian, Huber criteria.

I. INTRODUCTION

Breast Cancer (BC) is a genetic malignancy and is the second most common cause of cancer-related fatalities in women worldwide [1], [2]. The Global Breast Cancer Initiative (GBCI) intends to reduce world breast cancer deaths by 2.5% every year, potentially averting 2.5 million deaths from 2020 to 2040 [3], [4]. Generally, the abnormal growth of cells in the human body progresses into tumors and becomes lethal if untreated [5]. This necessitates early detection and diagnosis of BC to improve survival rates, minimize aggressive treatments, and reduce the risk of metastasis [6]. Globally, cancer diagnosis involves tissue extraction by biopsies, followed by histopathological evaluation to detect cellular abnormalities, and is supplemented by advanced imaging techniques to determine tumor location, morphology, and progression. Particularly, invasive biopsies insist on needle insertions or surgical tissue removal, while non-invasive imaging methods are patient-friendly [7]. Non-invasive imaging methods mammography [8], [9],

The associate editor coordinating the review of this manuscript and approving it for publication was Qiang Li.

ultrasound [10], [11], [12], Computed Tomography (CT) [13], [14], Digital Tomosynthesis [15], and Magnetic Resonance Imaging (MRI) [16], [17] aid in assessing the tumor heterogeneity and monitoring treatment response. Unlike the abovementioned modalities, which capture anatomical information, DCE-MRI provides intriguing insights into tissue vascularity and perfusion with high temporal and spatial resolution [18], thereby refining tumor segmentation. However, owing to intricate tumor biology and inconsistent intensity variations, tumor segmentation remains challenging and demands a robust model for precise tumor delineation.

Traditionally, the widely popular Active contours [19], [20], [21] segmented tumors by exploiting pixel characteristics to localize the precise ROI. However, their dependence on localized pixel characteristics for image decomposition hinders their ability in complex imaging scenarios like DCE-MRI [22], [23]. These setbacks led to the development of data-centric approaches to capture tumor heterogeneity and refine boundaries by learning patterns from the input image. Consequently, the advent of machine learning encouraged the development of data-driven approaches [24], [25], [26], [27], [28] that adaptively assess the pixel information to refine ROI, regardless of their inherent noise, intensity variations, and heterogeneous tumor shapes. Furthermore, the trending deep learning (DL) models U-Net [29], [30], nn-UNET [31], FCN [32], Att-U-Net [33], Swin Transformer [34], and Att-U-Node [35] learn complex pixel patterns from tumor with varying shapes and size ensuring spatial consistency. However, the empirical choice of regularization and optimization adopted in these models often leads to inconsistent interpretability and generalization. Moreover, the model's dependency on a large amount of labeled data and high-performance computing resources results in reduced scalability, high cost, and limited accessibility. To address these challenges, this work adopts a contextual regularizer-based optimizer to prioritize the contour pixels from non-contour ones for precise tumor delineation. An adaptive regularizer engages a minimax-concave penalty term that effectively balances the sparse and dense regression by modulating its impact on tumor and non-tumor regions. Accordingly, the model's cost function employs two energy-tuned data fidelity terms and a contextual adaptive regularizer arranged in a non-linear convex form. Also, the characterization of energy terms using the derivative images (Hessian) captures the local curvature of the tumor by refining the ridges and edges. Later, the variational minimax optimizer either maximizes or minimizes the cost by tuning the weights imposed by the contextual regularizer to attain the global optima, achieving improved sensitivity and robustness in tumor segmentation.

The rest of the paper is sectioned as follows: An extensive review of the traditional and trending breast tumor segmentation models is done in Section II, followed by CRBEO characterization in Section III. Section IV describes the datasets and metrics utilized for analysis, while Section V qualitatively and quantitatively analyzes CRBEO.

The ablation study and the complexity analysis of the CRBEO are presented in Sections VI and VII, followed by the conclusion outlining future directions in Section VIII.

II. RELATED WORKS

Efficient BC diagnosis relies on precise tumor segmentation and has remained a significant research area over the past few decades. Despite advancements in imaging modalities, an accurate and reliable segmentation tool is still challenging owing to factors such as intricate tissue characteristics, intensity variations between tumor and surrounding tissues, and image artifacts. To address these issues, a wide range of techniques were developed spanning from traditional segmentation methods to more sophisticated machine learning and deep learning techniques. Accordingly, this section chronologically reviews traditional and recent DL segmentation models outlining their pros and cons to highlight the novelty of the developed model.

Traditionally, the widely popular Active Contour Models (ACMs) optimize an energy function based on image gradients and pixel characteristics to segment image boundaries in a curvilinear fashion. While ACMs have been the foundation for segmentation tasks, their limitations in handling complex and heterogeneous DCE-MRI make them less effective for breast tumor segmentation. However, ACM variants [19], [20], [21] overcome these discrepancies by refining the curvilinearity. Nevertheless, its adaptation to the complex tumor shape, initial parameter tuning, and computational cost restricts its application in the complex DCE-MRI environment. For instance, the level-set segmentation [36] fitted a signed pressure function to address the weak edges present in the background ensuring robust segmentation. However, the model failed to generalize to various tumor types and imaging conditions. Alternatively, the Spectral embedding-based active contour (SEAC) [37] efficiently segmented tumors by engaging a local-global approach from the temporally organized DCE-MRI. This automated SEAC eased diagnostics with improved clinical settings and alleviated labor-intensive annotation. However, its reliance on parameter initialization and the quality of time-series data down-weighed its efficiency. Likewise, the unified energy functional [38] performed segmentation with registration by dynamically exploiting the statistics of intensity curves within homogeneous regions and discarded the heterogeneous variations. Nonetheless, the model's insensitive nature led to false delineations that augmented the non-tumor regions across the boundaries, leading to pixel imbalance. Another variant background distribution-based active contour model using level set (BDACMLS) [39] adopted a signed pressure function that subjectively selected the intensity distribution in the ROI. The homogeneous background intensity distribution model failed to recognize tumors with complex shapes or varying intensities. In contrast, the other variant blended Otsu thresholding with region-growing to initially contour the breast region followed by ACM to precisely localize the ROI. Although this framework

dominated, the initial segmentation was incoherent with the second stage ACM [40]. Another framework [41] outlined a derivative-free Active Contour model Without Edges in GPU for enhancing real-time segmentation. However, the validation on limited subjects doubted its performance. Likewise, the semiautomatic breast segmentation model GrowCut (GC) with cancer-specific multi-parametric Gaussian Mixture Model (GCGMM) [42] performed interactive segmentation model that extremely relied on the expert's delineated outputs, which undervalued its performance. The other breast tumor segmentation framework delineated tumors using the ACM supporting automation [43] and registered superiority. Another ACM variant, integrated fuzzy-C-means clustering [26] addressed the blurred boundaries issue present in low-contrast and inhomogeneous intensity regions using an extreme learning framework.

Recently, Deep Learning approaches have gained significant attention across various domains owing to their ability to learn from the data and support decision-making with exceptional accuracy. Subsequently, the scores of DL-based DCE-MRI segmentation models leveraging high spatial and temporal resolution in outlining tumors were dealt with and discussed here.

At the onset, the reinforcement sampling strategy adopted in mask-guided hierarchical learning (MHL) [44] mitigated class imbalance by emphasizing tumor regions. Despite reducing false positives, the model efficacy relied on the quality of the initial mask. Contrastingly, the attention-guided joint-phase-learning network [45] captured dynamic contrast variations and tumor heterogeneity utilizing five separate streams that prioritized the tumor boundary and suppressed the background noises. However, its reliance on high-quality data and complex framework settings limits model optimization for various clinical applications. Another multichannel image representation model engaging 2D and 3D convolutional network (M2D3D-MC) [46] enhanced the contrast between lesions and surrounding tissues for precise tumor delineation. The merged 2D and 3D convolutional layers leveraged contextual information obtained from adjacent slices. Despite the quality improvement, establishing optimality between 2D and 3D convolution led to suboptimal feature fusion, affecting segmentation accuracy. The other attention network, tumor-attentive segmentation-guided Generative Adversarial Network [47] utilized a modified U-net generator with two discriminators to delineate tumor boundaries and enhance the feature representation. The adversarial operation mode over-simplified tumor representation downed the model accuracy. Another, two-stage U-Net [48] model precisely segmented the ROI and eliminated irrelevant non-tumor tissues using a Transformer module. The local and global receptive fields improved segmentation accuracy however, the processing two-stage U-net increased the inference time. Likewise, the ensemble U-Net model [29] sequentially processed the pre-contrast and two post-contrast images to address the class imbalance by ensuring equal participation of positive (lesion) and negative (background) patches that refined the ROI. The dimensions of multiple time series data and the demand for high-quality contrast images increased the model complexity.

Lately, the hemodynamic knowledge-based model [49] exploited the intensity variations of blood flow dynamics for characterizing tumor vascularization in DCE-MRI. This approach combined pharmacokinetics with dynamic contrast-enhanced prior (DCP) loss function that enhanced segmentation quality. These improvements were paid at the expense of increased computational cost and data dependency. The tumor-sensitive synthesis module [50] suppressed false positives using a recursive differential loss function that precisely discriminated the pixels representing tumor regions. However, this model was sensitive to image quality, and over-suppression of false positives missed out on minuscule tumor information which is deemed essential for segmentation. Another Attention-guided U-Node with neural ordinary differential equation (ODE) [35] utilized the encoder-decoder model that enhanced feature refining with optimization at the cost of skipping connections. The iterative network incurred longer inference time as the ODE-based feature refinement process involved more computations. The other variant Progressive Dual Priori Network (PDPNet) [51] localized ROI by eliminating small intensity variations using weak semantic priors. The model's dependency on detailed prior knowledge and data over-smoothening declined the model's performance. The hybrid CNN module coupled with transformer architecture [52] utilized prototype learning to increase the segmentation accuracy. The model segmented tumors by learning biologically meaningful features rather than depending on pixel intensity. The apriori knowledge-based SwinHR engaged the hierarchically re-parametrization large kernel architecture (H-RLK) [34] to improve tumor segmentation. The dual-branch CNN network with Swin Transformer extracted contextual information that effectively addressed tumor heterogeneity and blurred boundary issues utilizing a shifted window mechanism. This property of the network improved the spatial resolution which is significant for dense and fine-grained prediction. However, these models fail miserably when dealing with small mesh lesions impacting their model accuracy. The recent edge-aware attention module (EAAM) [53] combines deep contextual features with edge features that lead to effective feature reasoning and information propagation. Although the model focused on refining boundaries, it over-emphasized the sharp edges and led to under-segmentation. The jointly operated DeepLabV3+ with modified ResNet50 [54] captured high spatial information by replacing the convolution layers with dilated convolutions. The combined network improves feature extraction and segmentation accuracy by engaging parallel convolutions. Also, the extensive diagnostic precision by leveraging more relevant and contextual feature extraction has extended the application of most recent DL models [55], [56] to detect and classify.

From the above discussion, all the DL models are bounded to pixel-wise fitting and typically serve as architectural templates to increase the efficiency of the model. Although these models improve segmentation accuracy, they lack interpretability and fail to extract meaningful insights vital for accurate medical diagnoses and treatment planning. Moreover, their dependency on the large volume of high-quality image data reduces their generalization capability. In contrast, CRBEO effectively refines the heterogeneous tumor boundaries by dynamically adapting the segmentation constraints based on tumor morphology and its pixel intensity captured by DCE-MRI. The model's reduced dependency on huge datasets and improved generalization make it suitable for medical applications where reliability and precision are deemed essential. Moreover, CRBEO's well-defined mathematical framework promotes transparency and assists validation in medical applications.

III. METHODOLOGY

A. CONTEXTUAL REGULARIZATION-BASED OPTIMIZATION SUPPLEMENTING TUMOR SEGMENTATION

Breast DCE-MRIs typically exhibit high-intensity variations due to temporal changes in contrast agent uptake, motion artifacts, and inherent signal inhomogeneity. These variations manifest as ambiguous tumor boundaries in the acquired images that are undifferentiable from the surrounding tissue, posing a significant challenge in accurate tumor delineation. Hence, this work introduces a novel segmentation model by exploiting the differentiation and decomposition aspects in the acquired data, easing the separation of the diverse breast constituents based on their energy variations. Thus, distinguishing the contours across boundary interfaces where the image intensities undergo drastic variations is achieved. Consequently, an energy optimization technique is designed by incorporating a contextual regularizer to facilitate data acceleration and retardation in refining ROI. The model initially decomposes the breast DCE-MRI based on its energy to accentuate the variations between the heterogeneous and homogeneous boundaries constituting the tumor and non-tumor regions. Finally, the introduced convex optimizer integrates energy-based data terms and a cost-driven contextual regularizer to penalize the data terms to ensure optimization stability. Based on the outlined discussions, an overview of the developed segmentation model is presented as a flow chart in Fig. 1.

Mathematical modeling of CRBEO based on Fig. 1 begins with the formulation of the energy-tuned convex optimizer in Eq.(1).

$$E(H; \beta) = (1 - \beta)^2 E_1(H) + 2\beta(1 - \beta)E_2(H) + \beta^2 E_3(H) \tag{1}$$

The energy terms E_1, E_2, E_3 in Eq.(1) are Hessian characterized representing the localized intensity variations across the contours, distinct regions, and their intersections respectively. Hessian characterization ensures the acquisition of pixel

variations across curvatures, differentiating the tumor from the surrounding tissues. Accordingly, the diverse energy terms are Hessian $H(x, y)$ modeled and weighed by β ranging from 0 to 1. Further, to capitulate the significant image ($I(x, y)$) intensity deviations the normalized Hessian given in Eq.(2) is adopted to constrain the values in the range (0,1).

$$H(x, y) = \frac{\left|\nabla^2 I(x, y)\right|}{\max \left|\nabla^2 I(x, y)\right|} \tag{2}$$

Eq.(2) represents the second-order partial derivatives of image intensity at each pixel. Based on the normalized Hessian, the first energy term (E_1) is formulated and presented in Eq.(3)

$$E_1(H) = \frac{1}{3} \iint (I(x, y) - H(x, y))^2 dx dy \tag{3}$$

The energy term $E_1(H)$ in Eq.(3) represents the edge energy present across high-curvature boundaries, where the Hessian exhibits larger deviations. The modeled $E_1(H)$ flattens the homogeneous intensity regions while highlighting the prominent edges and boundaries. To intensify the energy deviations further, the second energy term $E_2(H)$ is modeled in Eq.(4).

$$E_2(H) = \frac{1}{3} \iint (I(x, y) * H(x, y))^2 dx dy \tag{4}$$

Multiplying Hessian with the input image in Eq.(4) escalates the energies of high-frequency features that are vital for tumor segmentation. The energy models in Eq.(3) and Eq.(4) characterize the imbalanced pixels merging boundary regions with their surrounding areas and vice versa. Additionally, this imbalance contextually influences regularization, thereby warranting adaptive refinement during optimization. To achieve contextuality in regularization, CRBEO adopts the Huber-regularization model for driving the pixel outliers participating in segmentation.

1) HUBER-BASED REGULARIZATION

Huber-modeled regularization exploits the merits of the traditional $L1$ regularization promoting sparsity by penalizing large deviations, while $L2$ regularization smoothens data variations in homogeneous regions to achieve consistent segmentation accuracy when dealing with high-intensity variations. This arrangement highly suits segmentation where both smooth and sharp transitions are significant for distinguishing the tumor from its surrounding tissues. Accordingly, the third energy term $E_3(Huber)$ presented in Eq.(5) is Huber-modeled which contextually constrains the data terms by penalizing the rapid changes in the curvature boundaries during segmentation.

$$E_3(Huber) = \begin{cases} E_{\text{quadratic}} & \text{for } |\nabla H(x, y)| \leq \varepsilon \\ E_{\text{linear}} & \text{otherwise} \end{cases} \tag{5}$$
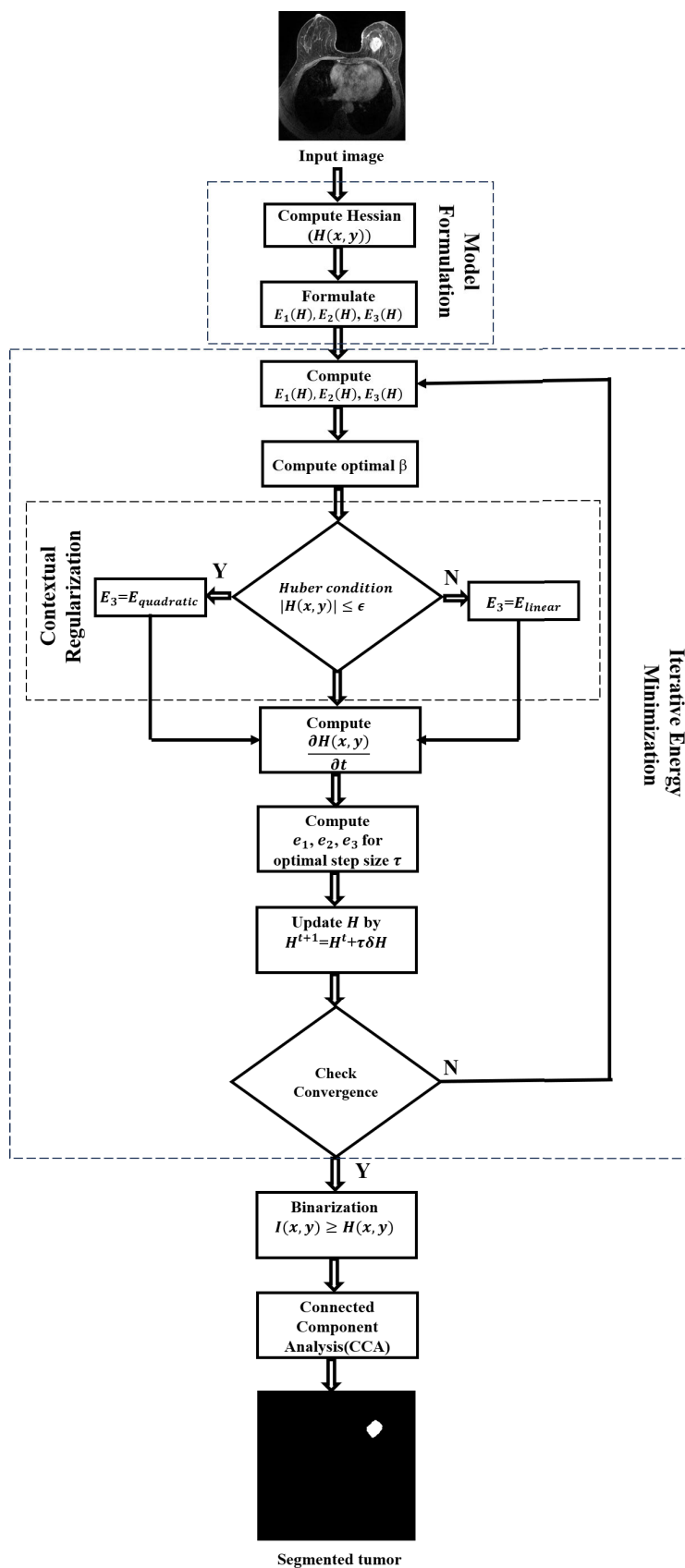
FIGURE 1. Flow diagram of CRBEO.

Herein $E_3(Huber)$ alternates between the quadratic and linear regularizers as expressed in Eqn. (6 & 7).

$$E_{\text{quadratic}} = \frac{1}{3} \iint \|\nabla H(x,y)\|^2 \, dx \, dy \tag{6}$$

The quadratic regularizer ensures the retainment of high-frequency variations by smoothening the homogeneous terms. Likewise, the heterogeneous variations are controlled by the linear term in Eq. (7).

$$E_{linear} = \frac{1}{3} \iint (2\varepsilon \, |\nabla H(x,y)| - \varepsilon^2) dx dy \tag{7}$$

The term ε defined in Eq.(8) ensures adaptive regularization whose magnitude drives Eq.(5) to $E_{\text{quadratic}}$ for smaller values else switches to E_{linear}.

$$\varepsilon = \frac{\alpha}{MN} \sum_{m=0}^{M-1} \sum_{n=0}^{N-1} |\nabla H(x,y)| \tag{8}$$

The Hessian characterized ε is normalized by the image dimensions and exceeds '1' owing to absolute operation, thereby insisting on bounding to avoid overfitting. Accordingly, the empirical parameter α introduced in Eq.(8) assumes either 0.1 or 1, weighing ε to oscillate between $L1$ or $L2$ regularization.

2) DUALITY PROPERTY

After contextually regularizing data, the model insists on minimizing the cost function $(E(H; \beta))$ to achieve efficient segmentation. Consequently, the dense variations in H are maximized by minimizing the β using the variational minimax principle, yielding a minimax solution for $\max_H \min_\beta E(H; \beta)$. The concave-convex nature of $(E(H; \beta))$ determines the existence and uniqueness of the solutions in the variational minimax problem. According to the minimax duality property, Eq.(9) depicts strong duality which is significant in obtaining robust energy optimization.

$$H^* = \arg \max_\beta \min_H E(H; \beta) = \arg \min_H \max_\beta E(H; \beta) \tag{9}$$

It is evident in Eq.(9) that the duality gap is zero [57] for this objective and it is desirable to interchange the order. Despite Eq.(9) being considered as a primal or dual perspective, the ideal solution requires reaching either the maximum or minimum, yielding the single optimum. The following sections detail the steps involved in finding the optimal weight parameter β, optimal H, and step size τ.

3) COMPUTING β

To compute optimal β, the cost function $(E(H; \beta))$ is differentiated with respect to β and equated to zero as $\frac{\partial E}{\partial \beta} = 0$. The optimal β, labeled β^*, is given in Eq.(10).

$$\beta^* = \frac{E_1 - E_2}{E_1 - 2E_2 + E_3} \tag{10}$$

Eq.(10) remains stable for minor fluctuations for identifying the critical points, ensuring adaptability and stability in smoother regions.

4) MODELING OPTIMAL H

Eq.(11) defines the rate of change of $H(x,y)$, capturing the spatial variations of energy function E for fixed β. Additionally, E_f shown in Eq.(12) represents the Euler-Lagrange differential equation which describes the necessary conditions for optimization and highlights the stability between the global and local energies.

$$H^* = \frac{\partial H(x,y)}{\partial t} = -E_f \tag{11}$$

where,

$$E_f = E_H - E_{H_x} - E_{H_y} \tag{12}$$

This variational arrangement ensures that the directional energy variations support a precise and reliable segmentation process. The individual terms in RHS of Eq.(12) are Hessian characterized as $H_x = \frac{\partial H}{\partial x}$, $H_y = \frac{\partial H}{\partial y}$ to yield $E_H = \frac{\partial E}{\partial H}$, $E_{H_x} = \frac{\partial E}{\partial H_x}$, and $E_{H_y} = \frac{\partial E}{\partial H_y}$. Consequently, the resulting E_f takes two forms as defined in Eq.(13) and Eq.(15) based on Huber criteria satisfying either $|\nabla H(x,y)| \leq \varepsilon$ or $|\nabla H(x,y)| > \varepsilon$ as detailed below.

Case (1): Upon $E_{(quadratic)}$ selection, the corresponding E_f and change in H are presented in Eqs.(13&14),

$$E_f = -\frac{2}{3}(1 - \beta^*)^2(I - H) + \frac{4}{3}(\beta^* - (\beta^*)^2)(I * H)$$
$$- \frac{1}{3}(\beta^*)^2(\nabla^2 H) \tag{13}$$

$$\frac{\partial H(x,y)}{\partial t} = +\frac{2}{3}(1 - \beta^*)^2(I - H) - \frac{4}{3}(\beta^* - (\beta^*)^2)(I * H)$$
$$+ \frac{1}{3}(\beta^*)^2(\nabla^2 H) \tag{14}$$

Case (2): Upon $E_{(linear)}$ selection, the corresponding E_f and change in H are presented in Eqs.(15&16),

$$E_f = -\frac{2}{3}(1 - \beta^*)^2(I - H) + \frac{4}{3}(\beta^* - (\beta^*)^2)(I * H)$$
$$- \varepsilon\frac{2}{3}(\beta^*)^2(\nabla H) \tag{15}$$

$$\frac{\partial H(x,y)}{\partial t} = +\frac{2}{3}(1 - \beta^*)^2(I - H) - \frac{4}{3}(\beta^* - (\beta^*)^2)(I * H)$$
$$+ \varepsilon\frac{2}{3}(\beta^*)^2(\nabla H) \tag{16}$$

5) FORMULATING STEP SIZE τ

Generally, the step size governs the degree of accuracy of the numerical solution. Smaller step sizes improve accuracy by allowing the numerical approach to capture the important details of the solution, whereas the large steps tend to converge rapidly and miss the optima. In the context of CRBEO, the smaller step sizes capture minuscule variations, whereas the large values neglect the vital information, leading to inaccurate segmentation. Hence, the selection of step size is imperative to achieve accuracy, stability, and efficiency for any numerical simulation. Accordingly, the exact line search method based on the gradient descent [58], [59] is adopted as

shown in Eq.(17).

$$E(H^{(i)} + \tau^{(i)}\delta H^{(i)}) = E_1 + E_2 + E_3 \qquad (17)$$

where,

$$E_1 = \frac{1}{3}(1 - \beta^{(i)})^2 \sum (H^{(i)} + \tau^{(i)}\delta H^{(i)} - I)^2 \qquad (18)$$

$$E_2 = \frac{2}{3}(\beta^{(i)} - (\beta^{(i)})^2) \sum \left[I * (H^{(i)} + \tau^{(i)}\delta H^{(i)}) \right]^2 \qquad (19)$$

The final term in optimization contextually selects either $E_{(quadratic)}$ or $E_{(linear)}$ for conditions $|\nabla H(x, y)| \leq \varepsilon$ and $|\nabla H(x, y)| > \varepsilon$ respectively, as in Eqs. (20 & 21).

$$E_{quadratic} = \frac{1}{3}(\beta^{(i)})^2 \sum \left\| \nabla(H^{(i)} + \tau^{(i)}\delta H^{(i)}) \right\|^2 \qquad (20)$$

$$E_{linear} = \frac{(\beta^{(i)})^2}{3} \sum (2\varepsilon \left| \nabla(H^{(i)} + \tau^{(i)}\delta H^{(i)}) \right| - \varepsilon^2) \qquad (21)$$

Based on the above formulation, the Taylor series expansion of Eq. (17) is quadratically arranged in terms of τ as in Eq.(22).

$$E(H^{(i)} + \tau^{(i)}\delta H^{(i)}) = e_1 + \tau^{(i)}e_2 + (\tau^{(i)})^2 e_3 \qquad (22)$$

where e_1, e_2 and e_3 are derived Eq.(23)-(28).

Case (1): $E_{(quadratic)}$ regularization

$$e_1 = \frac{1}{3}(1 - \beta^{(i)})^2 \sum (H^{(i)} - I)^2$$
$$+ \frac{2}{3}(\beta^{(i)} - (\beta^{(i)})^2) \sum (I * H^{(i)})^2$$
$$+ \frac{1}{3}(\beta^{(i)})^2 \sum \left\| \nabla H^{(i)} \right\|^2 \qquad (23)$$

$$e_2 = \frac{2}{3}(1 - \beta^{(i)})^2 \sum (H^{(i)} - I)\delta H^{(i)}$$
$$+ \frac{4}{3}(\beta^{(i)} - (\beta^{(i)})^2) \sum (I^2 * H^{(i)}\delta H^{(i)})$$
$$+ \frac{2}{3}(\beta^{(i)})^2 \sum \nabla H^{(i)} . \nabla(\delta H^{(i)}) \qquad (24)$$

$$e_3 = \frac{1}{3}(1 - \beta^{(i)})^2 \sum (\delta H^{(i)})^2$$
$$+ \frac{2}{3}(\beta^{(i)} - (\beta^{(i)})^2) \sum (I * \delta H^{(i)})^2$$
$$+ \frac{1}{3}(\beta^{(i)})^2 \sum \left\| \nabla \delta H^{(i)} \right\|^2 \qquad (25)$$

Case (2): $E_{(linear)}$ regularization

$$e_1 = \frac{1}{3}(1 - \beta^{(i)})^2 \sum (H^{(i)} - I)^2$$
$$+ \frac{2}{3}(\beta^{(i)} - (\beta^{(i)})^2) \sum (I * H^{(i)})^2$$
$$+ \frac{1}{3}(\beta^{(i)})^2(2\varepsilon \sum \left| \nabla H^{(i)} \right| - \varepsilon^2) \qquad (26)$$

$$e_2 = \frac{2}{3}(1 - \beta^{(i)})^2 \sum (H^{(i)} - I)\delta H^{(i)}$$
$$+ \frac{4}{3}(\beta^{(i)} - (\beta^{(i)})^2) \sum (I^2 * H^{(i)}\delta H^{(i)})$$
$$+ \frac{1}{3}(\beta^{(i)})^2(2\varepsilon \sum \nabla(\delta H^{(i)}) \qquad (27)$$

$$e_3 = \frac{1}{3}(1 - \beta^{(i)})^2 \sum (\delta H^{(i)})^2$$
$$+ \frac{2}{3}(\beta^{(i)} - (\beta^{(i)})^2) \sum (I * \delta H^{(i)})^2 \qquad (28)$$

After differentiating Eq.(22) and equating to zero, the optimal step size is derived as in Eq.(29),

$$\tau^{(i)} = -(e_2/2e_3) \qquad (29)$$

6) UPDATING H

Eq.(14) and Eq.(16) representing the explicit numeric schemes are discretized as in Eq.(30), where the solution for the next time step (H_{mn}^{t+1}) is calculated directly from the current time step (H_{mn}^{t+1}). This explicit arrangement ensures conditional stability with rapid convergence.

$$H_{mn}^{t+1} = H_{mn}^t + \tau^t(\delta H^t) \qquad (30)$$

where, τ is the adaptive step size, and t is the iteration number.

The above iterative process is algorithmized below,

Step 1: Formulate $H(x, y)$ and $E_1(H), E_2(H), E_3(H)$

Step 2: Repeat until convergence

a. Compute $H(x, y)$ and $E_1(H), E_2(H), E_3(H)$

b. Compute $\beta^* = \frac{E_1 - E_2}{E_1 - 2E_2 + E_3}$

c. Verify Huber's condition:

　If $|\nabla H(x, y)| \leq \varepsilon$

　　Decision: $E_3 = E_{quadratic}$

　else

　　Decision: $E_3 = E_{linear}$

d. Upon selecting E_3, compute $\frac{\partial H(x, y)}{\partial t}$

e. Compute e_1, e_2, e_3 for calculating optimal step size τ

f. Determine optimal $\tau = -(e_2/2e_3)$

g. Update $H^{t+1} = H^t + \tau^t(\delta H)^t$

B. HESSIAN-UPDATED BINARIZATION

Finally, based on the updated Hessian ($H^*(x, y)$), the input image ($I(x, y)$) is binarized as given in Eq.(31).

$$I_{binary} = \begin{cases} 1, & \text{for } I(x, y) \geq H^*(x, y) \\ 0, & \text{elsewhere} \end{cases} \qquad (31)$$

C. REMOVING NON-TUMOR REGIONS

The binarized image in Eq. (31) constitutes the tumor and non-tumor regions. However, for precise tumor segmentation, a residual removal step is incorporated to improve CRBEO performance. This is achieved by analyzing connected regions and retaining the largest connected components (tumor) in the binary image. Accordingly, the CCA (Connected component Analysis) is adopted post-binarization to discard the residual regions that remove the minimal connected components as depicted in Fig 2.
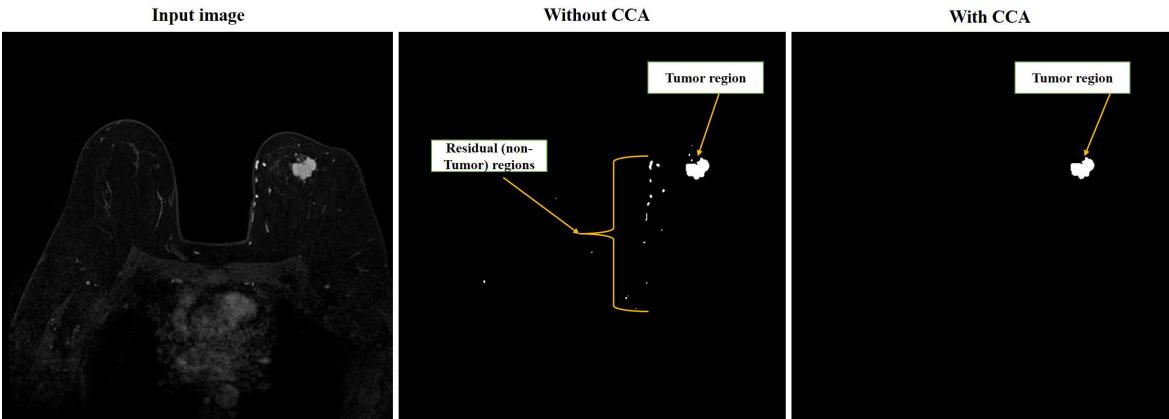
FIGURE 2. Representative DCE-MRI demonstrating the usage of CCA in the framework.

TABLE 1. Datasets description and imaging protocol.

Datasets/Parameters	Duke- Breast-Cancer-MRI	QIN breast DCE-MRI	TCGA BRCA	BreastDM	RIDER	ISPY1
Image strength	922	10	46	232	5	222
Scanner	1.5T GE	Siemens 3T	1.5T GE	3.0T GE	1.5T GE	3T GE &Siemens
Sequences	GRE	TWIST	3D spoilt gradient echo	VIBRANT	3D GRE	GRE
TR(ms)	3.54–7.39	2.9	***	4.7	***	8.4 & 3
TE(ms)	1.25–2.76	6.2	***	2.3	***	4.2 & 4
Flip angle (degree)	7–12	10	***	10	***	20 & 45
FOV(mm)	250-480	300-340	***	340x340	***	160-180
Slice thickness(mm)	1.04-2.5	1.4	2-3	2.4	1-5	2
Matrix size	320 x 320	320 x 320	512x512	512x512	288 × 288	256x256
Slice number	160	112-120	85-112	71-112	60	60 & 64
Tumor diameter(cm)	***	***	***	***	***	~3
Benign/malignant cases	***	***	***	85/147	***	***

*** Not reported

IV. DATASET AND EVALUATION METRICS

A. DATASET DESCRIPTION

The choice of datasets for evaluating CRBEO's performance under the purview of accuracy, when dealing with large datasets, intricate tumor complexities, and scalability. Accordingly, the following benchmarked datasets with their characteristics are selected for validation.

1) DUKE- BREAST-CANCER-MRI [60]

This dataset consists of a large, well-annotated collection of clinical notes, radiology, and pathology reports, widely used in radiogenomics to analyze prediction outcomes, and lesion detection in DCE-MRI. Achieving consistent performance with a huge collection of DCE-MRI data poses a significant challenge to several trending and benchmarked segmentation models.

2) QIN BREAST DCE-MRI [61]

This dataset is mainly utilized for decision-making in oncology through quantitative imaging schemes and effectively supports the development of data acquisition and validation. However, this dataset is packed with poor resolution and proves to be challenging, particularly in localizing tumors.

3) TCGA-BRCA [62]

The heterogeneous TCGA-BRCA consists of 500 specimens per cancer type, with diverse acquisition settings in terms

of manufacturers, protocols, and scanning modalities. This dataset is accumulated with tissues of diverse geographical subjects, exhibiting multiple lesions with intricate tumor characteristics.

4) BREASTDM [63]

This DCE-MRI dataset contains huge heterogeneous tumor cases with multiple lesions. Also, the varied tumor subtypes with their intricate intensity variations and poorly defined boundaries add complexity in differentiating tumors, thereby requiring improved imaging and computational tools for better detection and classification.

5) RIDER [64]

This modest dataset has a limited number of scans with low resolution, resulting in blurred boundaries. Despite this pitfall, the dataset is effectively employed in testing the models' robustness.

6) ISPY-1 [65]

ISPY-1 dataset is packed with multi-modal information including histopathology, clinical, and molecular profiling for predicting therapeutic response. Heterogeneous tumor boundaries and intensity variations, owing to the different scanner and imaging protocols, make the dataset challenging for tumor segmentation.

Another critical factor in choosing these datasets is their public availability which ensures transparency and reproducibility in research. However, these datasets are widely used in medical image segmentation serving as benchmarks for training and testing various SOTA models. Validating CRBEO on these datasets facilitates the relative comparison with existing methods and establishes its effectiveness and generalizability across different clinical contexts. Accordingly, the characteristics of the dataset and their imaging protocol are presented in Table 1.

B. EVALUATION METRICS

The Receiver Operating Characteristics (ROC) metrics define how accurately the model differentiates tumor and non-tumor regions. Accordingly, ROC metrics are calculated based on the True Positive (TP), False Positive (FP), True Negative (TN), and False Negative (FN). Assuming U as the segmented output, and V as the ground truth, the TP, FP, TN, and FN are defined as $U \cap V, \overline{U \cap V}, U \cap \overline{V}$, and $\overline{U} \cap V$ respectively. The metrics given in Eq. (32)-(41) formulated using the above parameters are employed for analyzing the model performance.

$$Accuracy = \frac{TP + TN}{TP + TN + FP + FN} \quad (32)$$

$$Dice = \frac{2TP}{2TP + FP + FN} \quad (33)$$

$$Jaccard = \frac{TP}{TP + FP + FN} \quad (34)$$

$$Precision = \frac{TP}{TP + FP} \quad (35)$$

$$Sensitivity = \frac{TP}{TP + FN} \quad (36)$$

$$Specificity = \frac{TN}{TN + FP} \quad (37)$$

To investigate CRBEO's strength in classifying the pixels representing the tumor and tumor regions, the mean Intersection over Union (mIOU) and mean average Precision (mAP) parameters defined in Eqs. (38 & 39) are adopted.

$$Mean\ IOU = \frac{1}{N} \sum_{i=1}^{N} \frac{TP_i}{TP_i + FP_i + FN_i} \quad (38)$$

$$mAP = \frac{1}{N} \sum_{i=1}^{N} AP_i \quad (39)$$

where n is the number of classes, and AP_i is the average precision for class i. Additionally, the Structural Similarity Index (SSIM) given in Eq.(40) is used for analyzing the structural retention capacity of the proposed model.

$$SSIM(x, y) = \frac{(2\mu_x \mu_y + c_1)(2\sigma_{xy} + c_2)}{(\mu_x^2 \mu_y^2 + c_1)(\sigma_x^2 + \sigma_y^2 + c_2)} \quad (40)$$

Likewise, the segmented output and its corresponding ground truth are compared using the Hausdorff distance [66], as shown in Eq. (41).

$$H(X, Y) = \max(h(X, Y), h(Y, X)) \quad (41)$$

where $h(X, Y) = \max_{x \in X} \min_{y \in Y} \|x - y\|$ and x and y are the edge points corresponding to X and Y respectively, and $\|.\|$ is the Euclidean norm. Generally, a lower distance corresponds to the closeness of segmented output and ground truth.

C. BASELINES FOR RELATIVE COMPARISON

The baselines adopted for relative analysis with their pros and cons are enlisted to understand the relevance of their utilization in this study.

1. Unet3D [35] - Efficiently captured complex spatial information from 3D data preserving fine details with better feature learning using skip connections. However, the model is less effective in handling highly heterogeneous tumors owing to its fixed receptive fields.

2. VNet [35]- Effectively learned residual features for capturing contextual and fine details. While leveraging residual connections in feature learning, it struggles with small-sized tumors as it tends to prioritize larger structures.

3. UNETR [35]- This transformer-based model engaged a local-global unique structuring method to capture crucial spatial information and offered improved performance. Nonetheless, demanded extensive training data with exhaustive computations for model optimization.

4. nnU-Net [35]- The self-configuring network adapted to various complex data sets with high tumor segmentation accuracy. However, it encounters data overfitting when dealing with smaller datasets.

5. U-Node3D [35]- The enhanced 3D UNET leveraged feature extraction by retaining essential spatial information. However, hyperparameter tuning incurs extensive training data with time, thereby impacting model convergence during optimization.

6. Att-U-Node3D [35]- This attention mechanism focussed on relevant regions, making boundary detection more accurate, while remaining highly sensitive to noise.

7. Random forest [63]- The tree-based classifier was effective on smaller datasets and lacked scalability when dealing with high-dimensional data.

8. FCN-50 [63]- This network extracted multi-scale features and improved accuracy at a low computational cost. However, limited depth restricts their capacity to capture intricate spatial information.

9. DeepLabV3-50 [63]- The powerful and scalable network performed semantic segmentation by capturing multi-scale contextual information using Spatial Pyramid Pooling. The model's lower feature extraction depth hampered its ability to handle highly heterogeneous tumor structures.

10. DeepLabV3-101 [63]- Extracted detailed and complex features for fine-grained segmentation with robustness from varying datasets. However, the model incurred high computational costs.

11. U-Net-VGG16 [63]- Blended U-NET with VGG16 for extracting highly localized features and ensured rapid convergence with improved accuracy. Nevertheless, the

model struggled to capture edge variability and is less efficient for small-sized tumors.

12. UNeXt [63]- Coupled EfficientNet with U-Net for tumor segmentation, offering enhanced flexibility and scalability, however demands rigorous parameter tuning when dealing with diverse datasets.

13. PSPNet [63]- Incorporated pyramid pooling for multi-scale feature extraction. However, the performance dropped when dealing with small tumors or irregular shapes.

14. 3D-DenseSeg [63]- Aimed at efficient semantic segmentation using powerful feature learning with propagation. However, the model failed when encountering tumors with complex data variations.

15. EEU-Net [67]- The improved U-Net extracted edge features by incorporating edge-enhanced feature learning for enhanced accuracy and was less effective when dealing with tumor heterogeneity and high noise levels.

16. PDP-Net [51]- The pixel-level feature discrimination network detected boundaries and performed dense object segmentation. This computationally demanding model struggled to generalize across different imaging modalities.

Primarily, the abovementioned baseline DL architectures deployed max-pooling or stride convolutions for downsampling which undergoes spatial resolution loss. This is particularly problematic for small tumors as critical details might be lost during segmentation. Moreover, their reliability on convolutional layers with fixed kernel sizes does not adequately capture global contexts that are important for heterogeneous tumors, and also the fine-grained details that are critical for small tumors. Finally, these models failed to capture irregular tumor boundaries as the employed standard convolutional filters are not designed to handle edge variability caused by irregular-shaped tumors.

V. RESULTS AND DISCUSSIONS

CRBEO's segmentation performance is studied under two contexts: a) self-analysis and b) relative analysis to effectively showcase its consistency and robustness in segmenting heterogeneous tumors. The Duke-Breast-Cancer-MRI dataset is adopted for self-analysis due to its intricate and high dimensional data. This analysis is significant in highlighting the model's strengths and its possible limitations, which are deemed essential for decision-making and future improvements. To proceed with the abovementioned validation, the ground truth for the Duke-Breast-Cancer-MRI dataset is annotated by an expert from the Department of Radiology, Cincinnati Children's Hospital Medical Center, Cincinnati, United States. Similarly, the relative analysis permits the comparative evaluation against the trending SOTA methods to identify the gaps that need development. This analysis is conducted on challenging datasets namely, the QIN breast DCE-MRI, TCGA-BRCA, BreastDM, RIDER Breast MRI, and ISPY-1. The subsequent sections describe both quantitative and qualitative analysis of CRBEO, considering various limitations across complex datasets.

A. SELF-ANALYSIS

To validate the boundary-refining ability of CRBEO, 120 breast cancer patients with different tumor grades (1,2,3) were chosen and delineated with the help of an expert. Accordingly, Fig. 3 is a column-wise visual with each column depicting input, ground truth, segmented output, and contour overlaid on the input image.

Fig. 3 shows that the segmented output in column 3 closely aligns with the annotated ground truth in column 2. Notably, grade 1 tumors show better precision owing to their clear boundaries and lower complexity. Contrastingly, grades 2 and 3 show slightly decreased accuracy, which is attributed to the tumor's invasive growth patterns and heterogeneous boundaries. These visuals prove that CRBEO effectively utilizes a concave-convex and contextual regularizer for precise boundary delineation. To further strengthen the claim, a detailed quantitative analysis of the segmentation performance over different tumor grades is performed using the evaluation metrics outlined in Eqs. (32)-(41) and presented in Table 2.

From Table 2, the increased accuracy (>99%) demonstrates the reliability of the CRBEO model in capturing more ambiguous boundaries, especially in higher-grade tumors. Also, the higher SSIM and HD95 signify the model's ability to retain structural integrity owing to its robust energy optimization technique, utilizing Huber criteria. Similarly, the Dice score and Jaccard highlight the strength in capturing spatial information across homogeneous regions of the tumor. The high mAP indicates that CRBEO has minimal false positives, thereby exhibiting superior precision in segmenting tumors.

B. RELATIVE-ANALYSIS

To evaluate the performance of CRBEO, a detailed comparative analysis against various existing SOTA methods was conducted to emphasize its adaptivity and boundary-refining ability. Accordingly, Fig. 4 depicts the segmentation outputs from QIN breast DCE-MRI and TCGA-BRCA datasets, demonstrating the multifocal tumor and its intricate intensity variations. Fig. 4 illustrates that the introduced Hessian-based contextual regularization efficiently adjusts to heterogeneous tumor morphologies, while the designed energy functionals precisely segment the boundaries even in asymmetrical, multiple, and irregular-shaped tumor cases. In particular, Fig. 4 (b & c) depicts the tumor from the TCGA-BRCA dataset, (b) with only primary lesions, and (c) with primary and secondary lesions. TCGA-BRCA dataset typically consists of primary lesions used for various genomic studies, where the ground truth for the secondary lesions is not available on the TCIA website. However, to achieve a comprehensive analysis of this dataset, the authors from [68] complemented the ground truth by including the secondary lesions. The model shows its superiority in differentiating primary and secondary tumors with its overlapping spatial configurations. Similarly, Fig. 5 (a, b &c)
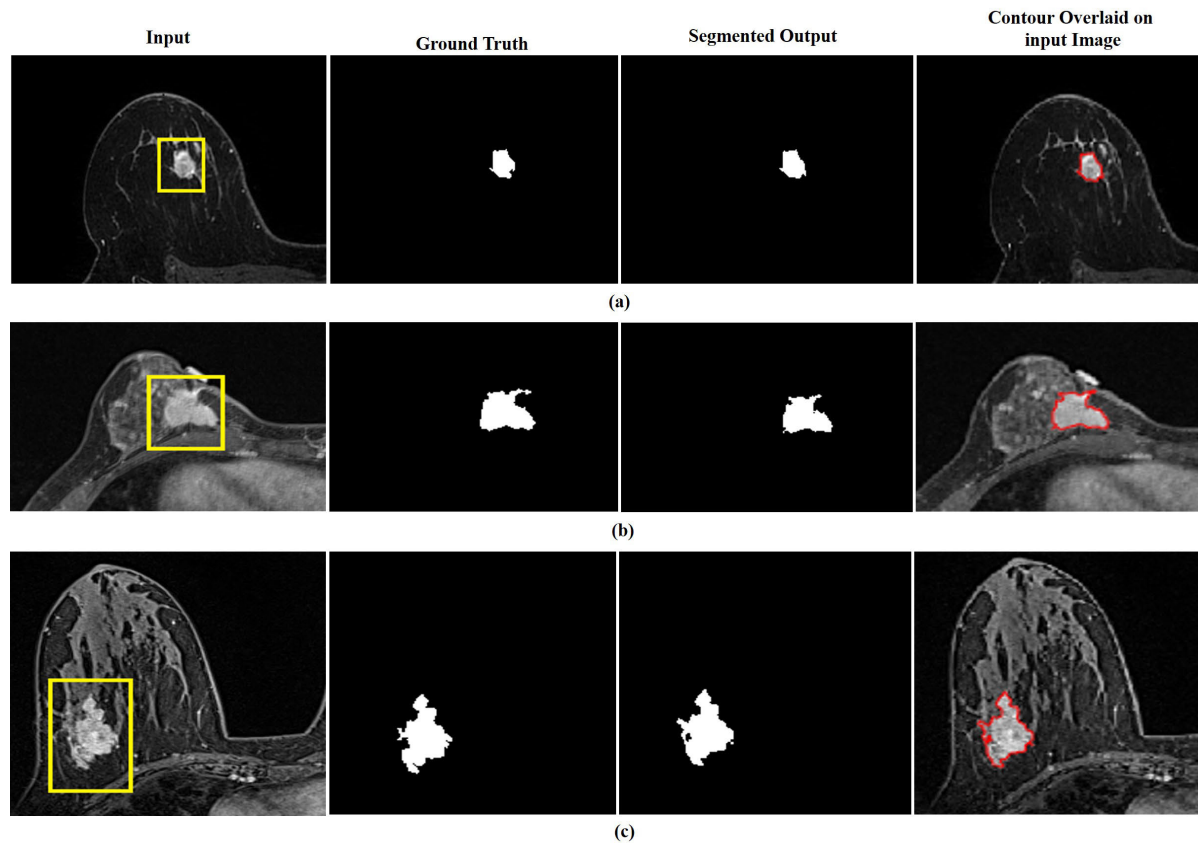
Input	Ground Truth	Segmented Output	Contour Overlaid on input Image

FIGURE 3. Representative axial DCE-MRI depicting grade-wise segmentation using CRBEO. (a) Grade 1, (b) Grade 2, (c) Grade 3.

TABLE 2. Quantitative analysis of CRBEO using Duke- Breast-Cancer-MRI.

Grades	Accuracy	Dice	Jaccard	mAP	Sensitivity	Specificity	SSIM	HD95
Grade 1	99.89	95.18	91.99	95.75	95.60	99.94	99.55	1.0093
Grade 2	99.88	94.31	90.83	94.34	94.91	99.92	99.52	1.0547
Grade 3	99.86	94.24	90.91	94.18	95.01	99.56	99.45	1.0824

shows the DCE-MRI representing the segmented output from BreastDM, RIDER Breast MRI, and ISPY-1 datasets respectively. The image organization adopted in Fig. 3 is extended to Fig. (4 & 5) depicting column 1 as input, column 2 as ground truth, column 3 as segmented output, and column 4 as contour overlaid images. A spiculated, irregular-shaped, and potentially malignant tumor case from the BreastDM dataset is shown in Fig. 5 (a). The major challenge in segmenting this tumor is its internal heterogeneity attributed to the highly vascularized and necrotic regions. However, the incorporated Huber-based regularization seamlessly preserves tumor structure and eliminates spurious segmentation, particularly in tumors with increased proliferation. Similarly, the DCE-MRI image slice displayed in Fig. 5 (b) is taken from the RIDER breast MRI dataset. The indistinct contrast between the tumor and its surrounding tissues in the slice necessitates image enhancement as one of the preprocessing steps during segmentation process. However, even without preprocessing the image, the CRBEO integrates spatial and gradient information around the tumor boundaries for precise tumor extraction. The results in row 2 and column 3 of Fig. 5 (b) prove that the segmented output is more precise than the ground truth, ensuring the model's ability to capture the tumor's asymmetrical nature. Similarly, the tumor in Fig. 5 (c) shows highly radiated spikes and possible features of an aggressive multifocal tumor. Nevertheless, the Hessian-based energy optimization makes CRBEO highly sensitive to the curvature dissimilarities to effectively capture these radiating spikes along the spiculated patterns. To substantiate the above-mentioned assertion, a challenging tumor case from QIN breast DCE-MRI [35] is selected and their masks generated by various SOTA methods are compared with the CRBEO model visually in Fig. 6.

Upon observing the input breast image in Fig. 6, the tumor appears with a well-circumscribed boundary and an unvaried intensity distribution, possibly a less invasive and low-grade tumor. This clear boundary across the tumor and non-tumor regions presents a challenge in delineating the
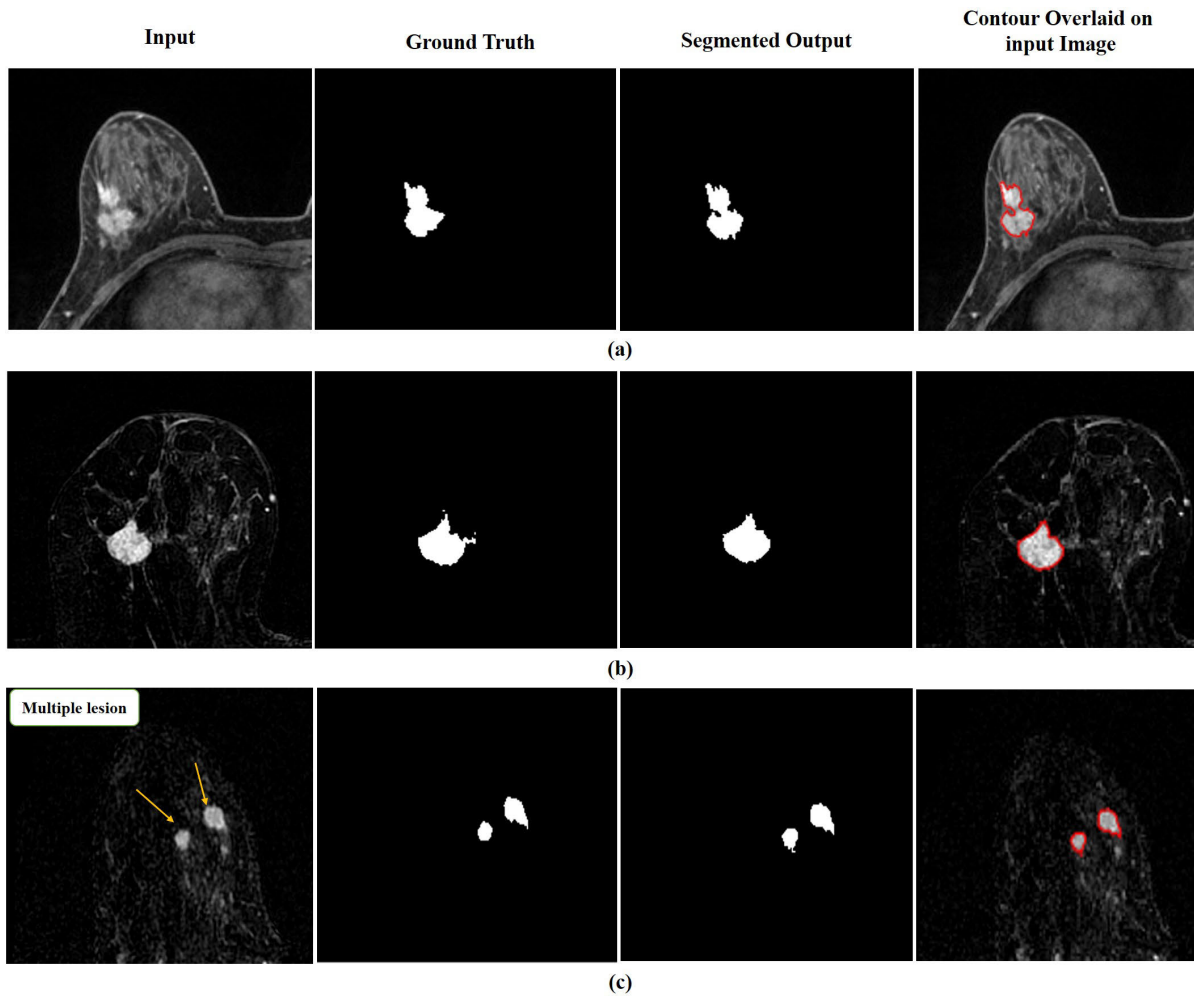
| Input | Ground Truth | Segmented Output | Contour Overlaid on input Image |

(a)

(b)

(c)

FIGURE 4. Representative DCE-MRIs demonstrating segmented output from various datasets. (a) QIN breast DCE-MRI, (b) TCGA-BRCA (primary lesion) (c) TCGA-BRCA (primary lesion + secondary lesion).

TABLE 3. Comparative analysis of CRBEO with various SOTA methods using QIN breast DCE-MRI dataset.

Method	Dice	Jaccard	Precision	Sensitivity	Specificity	HD95
UNet3D	64.84	52.10	73.07	74.64	99.13	18.57
VNet	65.49	51.45	72.34	72.76	99.46	16.67
UNETR	63.51	48.66	68.10	74.71	99.30	26.48
nnU-Net w/o *PP	61.07	49.01	67.13	74.43	99.42	19.04
nnU-Net w/*PP	63.35	51.47	69.72	74.43	99.55	12.88
U-Node3D	63.03	48.71	68.71	75.27	99.55	11.86
Att-U-Node3D	69.70	55.57	76.22	75.39	99.68	14.53
CRBEO	**87.26**	**80.62**	**88.82**	**94.12**	**99.90**	**3.67**

*PP-Post Processing

tumor as there is a chance for over-segmentation. Notably, the other SOTA models namely, VNET, UNETR, and nnU-NET have localized ROI, nevertheless, there is a small isolated non-tumor region which is misinterpreted as tumor tissue. This misinterpretation eventually leads to erroneous decision-making by the clinicians. In contrast, models like UNET3D, U-Node3D, and Att- U-Node3D have precisely segmented the tumor, however the former competitors have smoothed the boundaries and misaligned with the ground truth. CRBEO has perfectly capitulated and retained the boundaries by leveraging its adaptive and contextual regularization, which is well-suited for homogeneous and heterogeneous tumors.

Further to objectively validate CRBEO's performance, an extensive quantitative analysis was conducted using the evaluation metrics stated in Eqs. (32)-(41) and results are tabulated for each dataset. These metrics are chosen owing to the broad recognition and their compatibility with
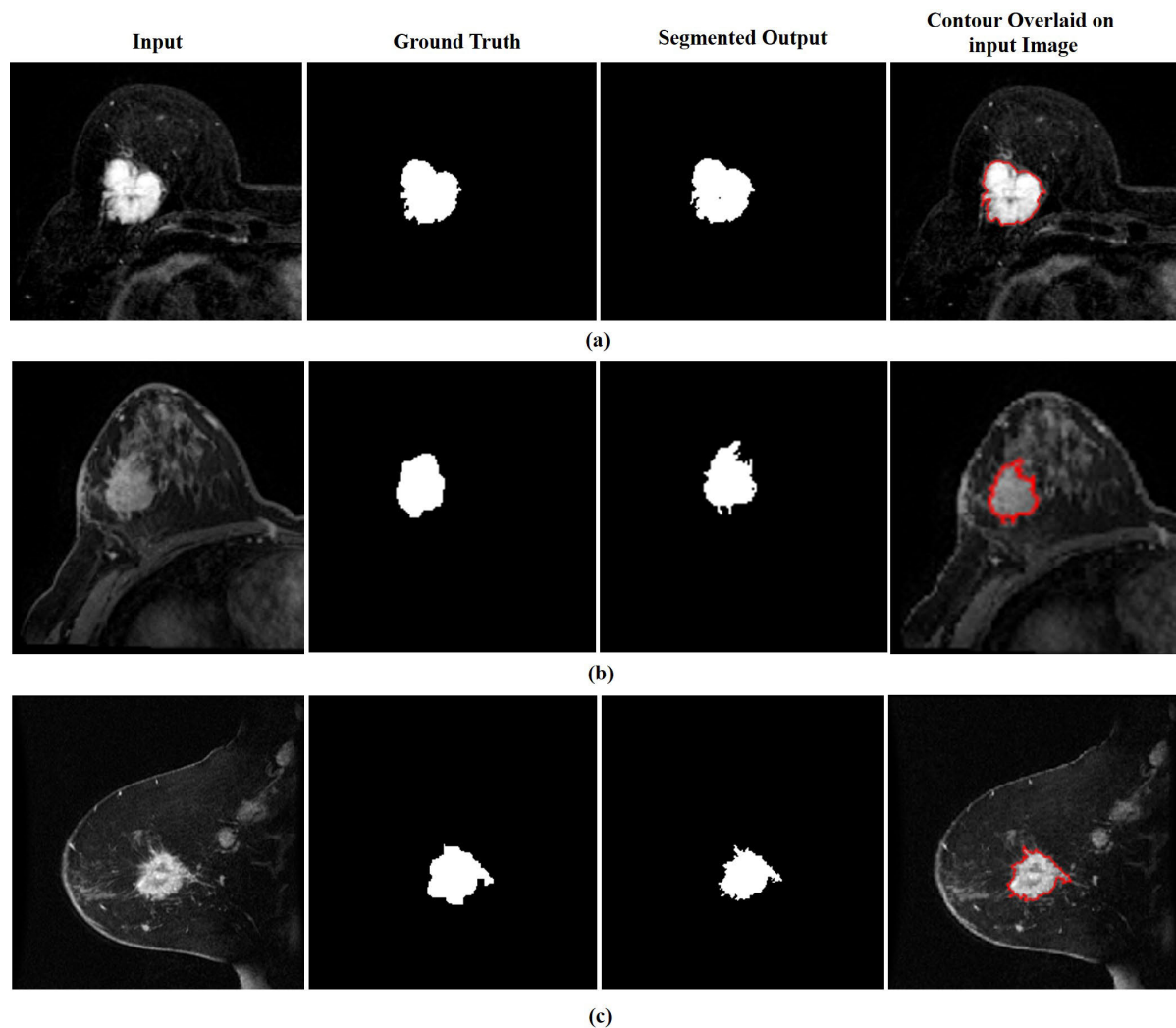
Input	Ground Truth	Segmented Output	Contour Overlaid on input Image

(a)

(b)

(c)

FIGURE 5. Representative DCE-MRIs demonstrating segmented output from various datasets. (a) BreastDM, (b) RIDER Breast MRI (c) ISPY-1.

trending SOTA methods, assuring a comprehensive and fair comparison. Also, the selected metrics yield an elaborate analysis related to structural retention, boundary description, and accuracy in the segmentation process. Accordingly, Table 3 illustrates the comparative analysis of the proposed CRBEO with the different SOTA methods using the QIN breast DCE-MRI dataset.

The bolded row in Table 3 is the segmentation results corresponding to the CRBEO model. Notably, the high Dice and Jaccard signify that the model exhibits superior boundary refining ability, exceeding all the black-box models. Also, the recorded sensitivity, specificity, precision, and HD95 values reflect the model's potential to prevent the inclusion of non-tumor regions, ensuring an increased true positive rate. This performance is due to energy optimization and Huber-based regularization, which enhances the adaptivity of the model to complex tumor morphologies. Additionally, the relative analysis is extended to the TCGA-BRCA dataset

TABLE 4. Comparative analysis of CRBEO with UNET using TCGA-BRCA dataset.

Method	Dice
UNET-Primary lesion	80.20
UNET-Secondary Lesion	68.00
CRBEO	**82.86**

and their outcomes are recorded in Table 4. From Table 4, it is evident that CRBEO exceeds the UNET model in capturing both primary and secondary tumors. UNET model exhibits a high dice value for primary tumors, whereas, for secondary tumors, the model misaligns and fails to delineate multiple lesions. To maintain consistency, the other ROC parameters Jaccard, Precision, Sensitivity, Specificity, SSIM, and HD are evaluated and recorded as 80.78%, 88.80%, 90.05%, 97.27%, 94.78%, and 3.052 respectively. The relative analysis has been extended to the Breast DM
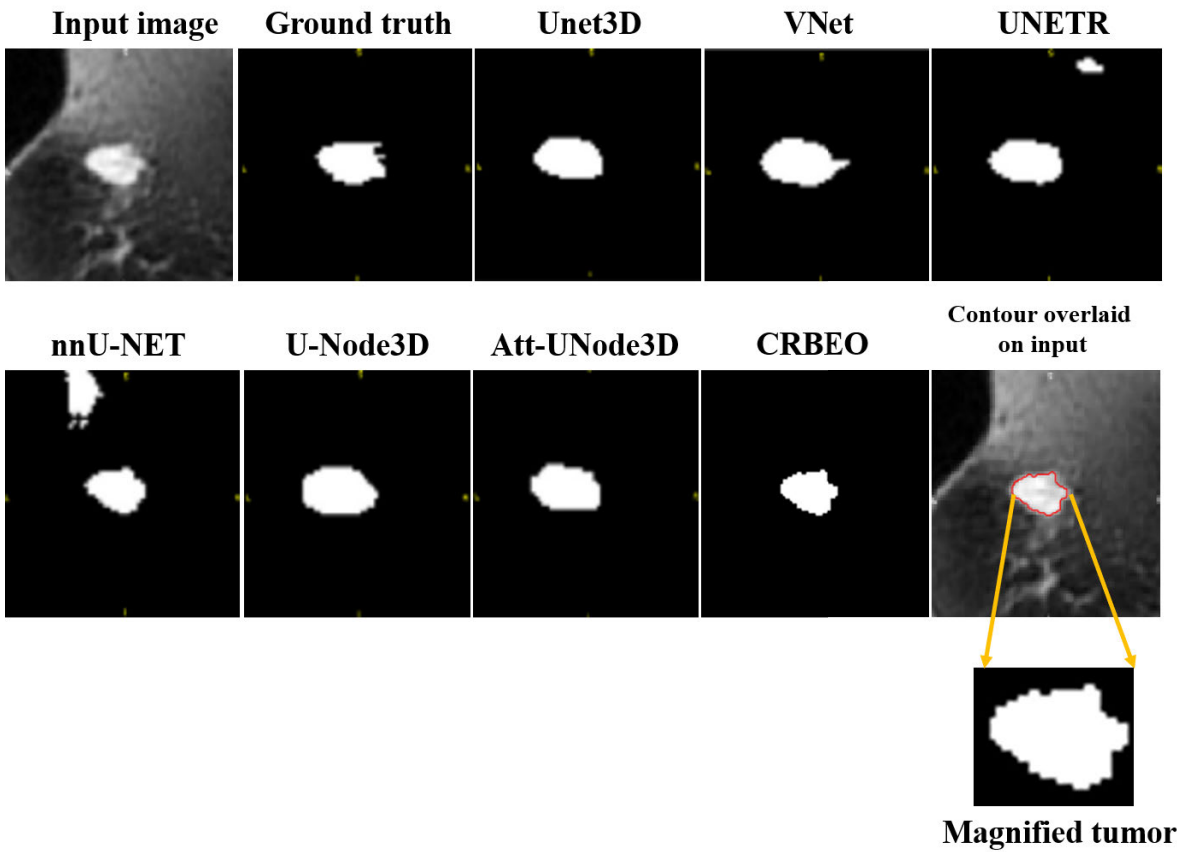
FIGURE 6. CRBEO comparison with various SOTA methods.

TABLE 5. Relative analysis of CRBEO with various SOTA methods using BreastDM dataset.

Method	Dice	mIOU	Precision
Random forest	66.2	74.5	75.3
FCN-50	71.1	77.7	77.0
FCN-101	71.4	79.0	76.2
DeepLabV3-50	72.9	79.3	80.3
DeepLabV3–101	73.4	78.7	86.5
Unet	73.7	80.3	83.6
Unet-VGG16	70.4	77.3	79.6
UNeXt	70.1	78.5	86.3
PSPNet	72.7	79.0	72.9
3DUnet	66.5	75.1	83.3
3DVnet	65.6	74.2	77.1
3D-DenseSeg	67.0	74.9	84.1
CRBEO	**86.17**	**88.24**	**89.24**

TABLE 6. Comparative analysis of CRBEO with EEU-NET using the RIDER dataset.

Method	Dice	Jaccard	Precision	Sensitivity	HD95
EEU Net	88.4	80.4	92.3	80.3	3.221
CRBEO	**89.3**	**82.6**	**91.8**	**87.1**	**1.106**

TABLE 7. Comparative analysis of CRBEO with PDP-NET using ISPY-1 dataset.

Method	Dice	Sensitivity	Specificity	HD95
PDPNet-(ISPY-G)	64.3	70.0	99.1	12.11
PDPNet-(ISPY-S)	43.3	44.3	99.6	22.74
CRBEO	**85.32**	**85.02**	**99.81**	**1.532**

dataset, wherein the peers have reported the Dice, Jaccard, and Precision values as depicted in Table 5. The above analysis is extended to the Breast DM dataset [63] wherein the peers have reported the Dice, Jaccard, and Precision values as depicted in Table 5. Table 5 reports a relative comparison of CRBEO's performance with various recent competitors. Moreover, the competitors [63] have engaged in spatial and intensity normalization as one of the preprocessing steps during segmentation. However, CRBEO discarded

spatial and intensity normalization and recorded superior Dice, mIOU, and Precision values than its predecessors. To demonstrate superiority, the other evaluation metrics Sensitivity, Specificity, SSIM, and HD are reported as 86.72%, 98.66%, 98.54%, and 1.186 respectively. Similarly, the relative analysis of CRBEO with EEU-NET was conducted and its performance is reported in Table 6. The potential challenge in the RIDER dataset is its low-resolution images obtained from limited scans. Upon analyzing Table 6, CRBEO exceeds performance in terms of Dice, Jaccard, sensitivity, and HD95, however, the precision value is slightly

TABLE 8. Wilcoxson signed test p-values: SOTA Methods vs. CRBEO using BreastDM dataset.

Methods	Random Forest	FCN-50	FCN-101	DeepLabV3-50	DeepLabV3-101	U-net	Unet-VGG16	UNeXt	PSPNet	3DUnet	3DVnet	3D-DenseSeg	CRBEO
Random Forest	1	0.7283	0.2707	0.7394	0.6627	0.1669	0.4825	0.8654	0.6735	0.0678	0.2973	0.7506	**0.0010**
FCN-50	0.7283	1	0.4643	0.7394	0.5997	0.1580	0.3329	0.7283	0.9823	0.3403	0.4464	0.7958	**0.0007**
FCN-101	0.2707	0.4643	1	0.2707	0.1624	0.0251	0.06567	0.2398	0.4553	0.6627	0.9942	0.5395	**0.0001**
DeepLabV3-50	0.7394	0.7394	0.2707	1	0.947	0.2973	0.6735	0.8418	0.5592	0.07013	0.2643	0.6100	**0.0021**
DeepLabV3-101	0.6627	0.5997	0.1624	0.947	1	0.4464	0.9234	0.7731	0.3871	0.0377	0.1858	0.4825	**0.0019**
U-net	0.1669	0.158	0.0251	0.2973	0.4464	1	0.5201	0.1907	0.0904	0.0687	0.0232	0.1335	**0.0215**
Unet-VGG16	0.4825	0.3329	0.0656	0.6735	0.9234	0.5201	1	0.4825	0.2772	0.0162	0.0656	0.2707	**0.0042**
UNeXt	0.8654	0.7283	0.2398	0.8418	0.7731	0.1907	0.4825	1	0.6414	0.0877	0.2643	0.6735	**0.0015**
PSPNet	0.6735	0.9823	0.4553	0.5592	0.3871	0.0904	0.2772	0.6414	1	0.1715	0.5298	0.9705	**0.0005**
3DUnet	0.0678	0.3403	0.6627	0.07013	0.0377	0.0687	0.0162	0.0877	0.1715	1	0.7065	0.2772	**0.0014**
3DVnet	0.2973	0.4464	0.9942	0.2643	0.1858	0.0232	0.0656	0.2643	0.5298	0.7065	1	0.5395	**0.0009**
3D-DenseSeg	0.7506	0.7958	0.5395	0.61	0.4825	0.1335	0.2707	0.6735	0.9705	0.2772	0.5395	1	**0.0005**
CRBEO	**0.0010**	**0.0007**	**0.0001**	**0.0021**	**0.0019**	**0.0215**	**0.0042**	**0.0015**	**0.0005**	**0.0014**	**0.0009**	**0.0005**	1

TABLE 9. Ablation study using Duke and QIN breast DCE MRI datasets.

Dataset	Methods	Dice	Jaccard	Precision	Sensitivity	Specificity	SSIM	HD95
Duke- Breast-Cancer-MRI	Without Huber regularization	88.50	84.43	92.90	85.37	99.21	98.76	1.656
	CRBEO	**94.57**	**91.24**	**96.31**	**95.17**	**99.44**	**99.05**	**1.0488**
QIN breast DCE-MRI	Without Huber regularization	83.12	77.89	85.28	88.45	98.78	98.23	3.73
	CRBEO	**87.26**	**80.62**	**88.82**	**94.12**	**99.90**	**99.92**	**3.67**

lower than the EEU Net model [67]. The rationale for the dip in the precision is due to the preprocessing step, as the EEU net model depends on image denoising and image contrast enhancement to improve image quality. In addition, dataset augmentation was performed to increase the samples for training the EEU-NET model. However, the Dice improvement of 1.012% without preprocessing, indicates that CRBEO is consistent and adaptive to low-quality images.

Likewise, Table 7 shows the relative analysis of CRBEO with PDP-NET [51] using the ISPY-1 dataset. Although this net progressively improves the prediction by incorporating spatial and contextual information, it insists on several preprocessing steps such as zero mean normalization and data augmentations engaging translation, scaling, and rotation during the training phase. Despite, the several preprocessing stages and the data augmentation in the training and testing stages, the model has recorded declined ROC values when compared to CRBEO. This improvement is attributed to the Huber-based regularization, which selectively makes a trade-off between data sparsity and smoothness by engaging L1 and L2 regularization.

Additionally, to validate the statistical significance, the Wilcoxon signed-rank test is performed with a significance level (α) of 0.05 on the BreastDM dataset, as it has been relatively compared with huge SOTA methods. The statistical outcomes are recorded in Table 8.

The bolded row in Table 8 shows the significant difference between the CRBEO and various SOTA methods. From the recorded p-values, it is observed that CREBO achieves better performance with consistency and remarkable

improvements over the SOTA methods on the BreastDM dataset. The incorporated contextual regularizer and adaptive energy optimization in CRBEO surpasses the trending DL and Machine Learning models in the segmentation process.

VI. ABLATION STUDY

To further establish the potential of the diverse modules constituting CRBEO, an ablation study was conducted using DCE-MRIs obtained from Duke breast MRI and QIN breast MRI, and the results are recorded in Table 9. The rationale for selecting these datasets accounts for their huge collection and distinct tumor characteristics. Table 9 shows the comparative results in two contexts, without Huber and with Huber (CRBEO) evaluated using the ROC metric stated in Eq. (32)-(41). The ROC metrics in Table 9 depict that the model performs well without Huber regularization, however, it misses out on finer details corresponding to tumor boundaries, leading to a decline in structure retention. Although Hessian individually demonstrates consistency across the ROC spectrum, the consistency with further improvement is witnessed when the model is coupled with Huber regularization. The blending of the feature characterizer with the contextual regularizer potentially differentiates the tumor and non-tumor regions. Although the image characteristics in both datasets are highly different, the analytical combination ensured higher achievements with consistency irrespective of the image variations.

To further claim CRBEO's simplicity and its extension to real-time applicability, its computational complexity is analyzed and presented below.

TABLE 10. Architecture and hardware details of various SOTA methods.

Architecture	Model training details	Hardware details	Time Complexity
3D U-NET [69]	Loss function: weighted softmax Optimizer: SGD Momentum: 0.99 Learning Rate: 0.01 Batch size: 1 Image size: 132x132x132	NVIDIA Titan X GPU (12 GB)	$O(L \cdot n \cdot k^3 \cdot c)$
3D V-NET [70]	Loss function: dice coefficient loss Optimizer: SGD Momentum: 0.9 Weight decay: 10^{-4} Batch size: 1 Image size: 128x128x64	NVIDIA Titan X GPU (12 GB)	$O(L \cdot n \cdot k^3)$
UNETR [71]	Loss Function: Dice Loss + Cross-Entropy Optimizer: AdamW Initial LR: 10^{-4} Weight Decay: 10^{-5} Batch Size: 2 Input Size: 96×96×96	NVIDIA A100	$O(L \cdot n^2)$
nnU-Net[72]	Loss Function: Dice Loss + Cross-Entropy Optimizer: SGD Momentum: 0.99 Weight Decay: 3×10^{-5} Batch Size: 2-4 Image size: 128×128×128	NVIDIA RTX 2080 Ti, RTX 3090, A100 (11 GB)	$O(L \cdot n \cdot k^3 \cdot c)$
Att-U-Node[35]	Loss Function: Dice Loss + Cross-Entropy Optimizer: SGD Learning Rate: 0.03 Batch Size: 12 Weight Decay: 5×10^{-4} Input Size: 512×512	NVIDIA GTX 2080Ti (11 GB)	$O(L \cdot n^2)$
FCN[73]	Loss Function: Pixel-wise Softmax Cross-Entropy Optimizer: SGD Learning Rate: 1×10^{-10} Momentum: 0.9 Image Size: 500×500	NVIDIA Tesla K20/K40	$O(L \cdot n \cdot k^2 \cdot c)$
DeepLabV3[74]	Loss Function: Pixel-wise Softmax Cross-Entropy Optimizer: SGD Momentum: 0.9 Learning Rate: 0.007 Image Size: 513×513	NVIDIA Tesla K80	$O(L \cdot n + n^2)$
PSPNet[75]	Loss Function: Pixel-wise Softmax Cross-Entropy Optimizer: SGD Learning Rate: 1×10^{-2} Batch Size: 16–32 Image Size: 473×473	NVIDIA Tesla P40	$O(L \cdot n + P \cdot n)$
UNeXt[76]	Loss Function: Dice Loss + BCE Loss Optimizer: Adam Learning Rate: 1×10^{-3} Image Size: 224×224	NVIDIA RTX 3090	$O(L \cdot n \cdot k^2 \cdot c)$
3D-DenseSeg[77]	Loss Function: Dice Loss Optimizer: Adam Learning Rate: 1×10^{-4} Batch Size: 1–2 Volume Resolution: 128×128×128	NVIDIA Tesla P100	$O(L \cdot n \cdot k^3)$
EEU net[67]	Loss Function: Dice Loss + BCE Loss Optimizer: Adam Learning Rate: 1×10^{-3} Input Resolution: 256×256	GPU with 32 GB RAM	$O(L \cdot n \cdot k^2 \cdot c)$
PDP NET[51]	Loss Function: Log-Cosh Dice Loss Optimizer: SGD Learning Rate: 0.001 Image Size: 128×128	NVIDIA Tesla P40	$O(L \cdot n \cdot k^2 \cdot c)$
CRBEO	**Loss Function: Energy function + Huber regularization** **Optimizer: Variational Minimax** **Image Resolution: 320×320, 512×512, 288×288, 256×256**	**Intel Core i5-1135G7 @ 2.40GHz**	$O((t \cdot m \cdot n)^2)$

VII. COMPUTATIONAL COMPLEXITY

CRBEO's complexity is analyzed in two distinct dimensions: (1) time complexity, which quantifies the asymptotic runtime of each module, and (2) space complexity, which constitutes the memory incurred during segmentation. The time complexity expressed in Eq. (42) represents the total computational cost incurred by CRBEO to achieve precise segmentation.

$$TotalTime = \sum_{i=1}^{N} T_i \approx T_{\max} \tag{42}$$

where, T_i represents the time complexity of each module, N is the total number of processing modules, and $T_{\max}$ refers to the maximum time complexity among all modules. For an image of size *mxn*, the computational complexity for calculating the three energy components is $O((tmn)^2)$, wherein t represents the number of iterations specific to each image. The quadratic order computation arises owing to the Hessian calculation, which incurs the highest complexity among the other modules. In addition, computing optimal β, H, and τ requires the computation of $O(tmn)$ while updating H and convergence checks incur the same complexity. Finally, the binarization and connected component analysis (CCA) depend on the image size, resulting in a complexity of $O(mn)$. Upon considering these processing operations, the total time complexity obtained by the CRBEO is shown in Eq. (43).

$$
\begin{aligned}
Totaltime = {} & O((tmn)^2) + O(tmn) + O(tmn) \\
& + O(tmn) + O(tmn) + O(tmn) + O(mn) \\
& + O(mn) \approx O((tmn)^2)
\end{aligned}
\tag{43}
$$

Likewise, CRBEO's space complexity is $O(mn)$, which corresponds to the memory required to process the input image of size $m \times n$. Further to understand the relative time complexity of CRBEO with its peers, a table summarizing model training details, hardware and the time complexity of various SOTA is presented in Table 10. Herein the time complexity of the diverse DL schemes is characterized by the number of network layers (L) with their dimensions (H), the number of pixels/voxels in the input image (n = M × N × D), the kernel size (k) varying according to their dimensions 2D or 3D,and the number of feature channels represented by c. Also, the DL models in Table 10 are majorly characterized by their Width and Depth along the architecture, which influences the kernel size and the receptive field with the spatial dimensions. This escalates their complexity more when considering the number of layers. Especially, the number of layers (L) engaged in formulating their architecture determines the training and testing times running from hours to days. Although the time utilized increases the model's learning ability and reduces the inference time, it lacks parameter transparency which is deemed essential for clinical application and decision-making. However, CRBEO accomplishes the same within a shorter time and does not require such training and testing

procedures with specialized hardware. In addition, CRBEO is characterized by the quadratic order and represents a single-layer framework whose adaptivity solely relies on contextual regularization, and is computationally simpler than the benchmarked segmentation counterparts.

VIII. CONCLUSION

This work presents an automatic breast tumor segmentation framework aimed at extracting multifaceted and irregularly shaped breast tumors from DCE-MRI. The major contribution of this work is the introduction of contextual regularizer into the optimization model for tuning the Hessian-characterized energy functions to perform precise tumor delineation. This arrangement ensures the refinement of heterogeneous-shaped tumors by precise delineation with simultaneous suppression of non-tumor regions. Rigorous qualitative and qualitative investigations on publicly available QIN-breast DCE-MRI, TCGA-BRCA, BreastDM, RIDER, and ISPY1 datasets demonstrated the model's superiority with Dice improvements of 30.16%, 11.48%, 20.66%, 1.012%, and 28.107%, respectively, against the peers. Further, simplicity analysis in terms of time and space showcased CRBEO's reduced computations, owing to its minimal processing modules, and its mathematical framework ensures transparency. Also, CRBEOs' acute tumor refinement in extremely challenging scenarios suits clinical applications like surgical planning and therapy monitoring. Positively, the CRBEO's segmentation potential needs to be studied with other modalities like CT, PET, MRI, and US. Additionally, incorporating modules for grading tumors after segmentation would make CRBEO a resource-efficient architecture. Despite CRBEO's dominance, its quadratic order in calculating the Hessian matrix incurs a long inference time compared with learning-based methods.

REFERENCES

[1] V. F. Grabinski and O. W. Brawley, "Disparities in breast cancer," *Obstetrics Gynecol. Clinics*, vol. 49, no. 1, pp. 149–165, 2022.

[2] P. V. Bhardwaj, R. Dulala, S. Rajappa, and C. Loke, "Breast cancer in India: Screening, detection, and management," *Hematol./Oncol. Clinics*, vol. 38, no. 1, pp. 123–135, 2024.

[3] D. Trapani, O. Ginsburg, T. Fadelu, N. U. Lin, M. Hassett, A. M. Ilbawi, B. O. Anderson, and G. Curigliano, "Global challenges and policy solutions in breast cancer control," *Cancer Treat. Rev.*, vol. 104, Mar. 2022, Art. no. 102339.

[4] R. L. Siegel, K. D. Miller, N. S. Wagle, and A. Jemal, "Cancer statistics, 2023," *CA, A Cancer J. Clinicians*, vol. 73, no. 1, pp. 17–48, Jan. 2023.

[5] A. I. Baba and C. Câtoi, "Tumor cell morphology," in *Comparative Oncology*. Bucharest, Romania: Publishing House of the Romanian Academy, 2007.

[6] S. Bellhouse, R. E. Hawkes, S. J. Howell, L. Gorman, and D. P. French, "Breast cancer risk assessment and primary prevention advice in primary care: A systematic review of provider attitudes and routine behaviours," *Cancers*, vol. 13, no. 16, p. 4150, Aug. 2021.

[7] S. Iranmakani, T. Mortezazadeh, F. Sajadian, M. F. Ghaziani, A. Ghafari, D. Khezerloo, and A. E. Musa, "A review of various modalities in breast imaging: Technical aspects and clinical outcomes," *Egyptian J. Radiol. Nucl. Med.*, vol. 51, no. 1, pp. 1–22, Dec. 2020.

[8] H. Hussein, E. Abbas, S. Keshavarzi, R. Fazelzad, K. Bukhanov, S. Kulkarni, F. Au, S. Ghai, A. Alabousi, and V. Freitas, "Supplemental breast cancer screening in women with dense breasts and negative mammography: A systematic review and meta-analysis," *Radiology*, vol. 306, no. 3, Mar. 2023, Art. no. 221785.

[9] A. Bilal, A. Imran, X. Liu, X. Liu, Z. Ahmad, M. Shafiq, A. M. El-Sherbeeny, and H. Long, "BC-QNet: A quantum-infused ELM model for breast cancer diagnosis," *Comput. Biol. Med.*, vol. 175, Jun. 2024, Art. no. 108483.

[10] N. S. Winkler, "Ultrasound guided core breast biopsies," *Techn. Vascular Interventional Radiol.*, vol. 24, no. 3, Sep. 2021, Art. no. 100776.

[11] W. K. Cheung, K. J. Williams, K. Christensen-Jeffries, B. Dharmarajah, R. J. Eckersley, A. H. Davies, and M.-X. Tang, "A temporal and spatial analysis approach to automated segmentation of microbubble signals in contrast-enhanced ultrasound images: Application to quantification of active vascular density in human lower limbs," *Ultrasound Med. Biol.*, vol. 43, no. 10, pp. 2221–2234, Oct. 2017.

[12] W. K. Cheung, B. N. Shah, A. Stanziola, D. M. Gujral, N. S. Chahal, D. O. Cosgrove, R. Senior, and M.-X. Tang, "Differential intensity projection for visualisation and quantification of plaque neovascularisation in contrast-enhanced ultrasound images of carotid arteries," *Ultrasound Med. Biol.*, vol. 43, no. 4, pp. 831–837, Apr. 2017.

[13] D. Lother, M. Robert, E. Elwood, S. Smith, N. Tunariu, S. R. D. Johnston, M. Parton, B. Bhaludin, T. Millard, K. Downey, and B. Sharma, "Imaging in metastatic breast cancer, CT, PET/CT, MRI, WB-DWI, CCA: Review and new perspectives," *Cancer Imag.*, vol. 23, no. 1, p. 53, May 2023.

[14] A. Bilal, M. Shafiq, F. Fang, M. Waqar, I. Ullah, Y. Y. Ghadi, H. Long, and R. Zeng, "IGWO-IVNet3: DL-based automatic diagnosis of lung nodules using an improved gray wolf optimization and InceptionNet-V3," *Sensors*, vol. 22, no. 24, p. 9603, Dec. 2022.

[15] T. Onega, L. Abraham, D. L. Miglioretti, C. I. Lee, L. M. Henderson, K. Kerlikowske, A. N. A. Tosteson, D. Weaver, B. L. Sprague, E. J. A. Bowles, and R. M. Di Florio-Alexander, "Digital mammography and digital breast tomosynthesis for detecting invasive lobular and ductal carcinoma," *Breast Cancer Res. Treat.*, vol. 202, no. 3, pp. 505–514, Dec. 2023.

[16] N. Ab Mumin, M. T. Ramli Hamid, J. H. D. Wong, K. Rahmat, and K. H. Ng, "Magnetic resonance imaging phenotypes of breast cancer molecular subtypes: A systematic review," *Academic Radiol.*, vol. 29, pp. S89–S106, Jan. 2022.

[17] R. Thawani, L. Gao, A. Mohinani, A. Tudorica, X. Li, Z. Mitri, and W. Huang, "Quantitative DCE-MRI prediction of breast cancer recurrence following neoadjuvant chemotherapy: A preliminary study," *BMC Med. Imag.*, vol. 22, no. 1, p. 182, Oct. 2022.

[18] M. Kataoka, "Ultrafast DCE-MRI as a new tool for treatment response prediction in neoadjuvant chemotherapy of breast cancer," *Diagnostic Interventional Imag.*, vol. 104, no. 12, pp. 565–566, Dec. 2023.

[19] T. F. Chan and L. A. Vese, "Active contours without edges," *IEEE Trans. Image Process.*, vol. 10, no. 2, pp. 266–277, Feb. 2001.

[20] S. Krinidis and V. Chatzis, "Fuzzy energy-based active contours," *IEEE Trans. Image Process.*, vol. 18, no. 12, pp. 2747–2755, Dec. 2009.

[21] R. Goldenberg, R. Kimmel, E. Rivlin, and M. Rudzsky, "Fast geodesic active contours," *IEEE Trans. Image Process.*, vol. 10, no. 10, pp. 1467–1475, Oct. 2001.

[22] M. Srikham, "Active contours segmentation with edge based and local region based," in *Proc. 21st Int. Conf. Pattern Recognit. (ICPR)*, Nov. 2012, pp. 1989–1992.

[23] A. Pratondo, C.-K. Chui, and S.-H. Ong, "Robust edge-stop functions for edge-based active contour models in medical image segmentation," *IEEE Signal Process. Lett.*, vol. 23, no. 2, pp. 222–226, Feb. 2016.

[24] P. F. Felzenszwalb and D. P. Huttenlocher, "Efficient graph-based image segmentation," *Int. J. Comput. Vis.*, vol. 59, no. 2, pp. 167–181, Sep. 2004.

[25] D. Mahapatra, "Analyzing training information from random forests for improved image segmentation," *IEEE Trans. Image Process.*, vol. 23, no. 4, pp. 1504–1512, Apr. 2014.

[26] B. Feng, H. Zhou, J. Feng, Y. Chen, Y. Liu, T. Yu, Z. Liu, and W. Long, "Active contour model of breast cancer DCE-MRI segmentation with an extreme learning machine and a fuzzy C-means cluster," *IET Image Process.*, vol. 16, no. 11, pp. 2947–2958, Sep. 2022.

[27] A. B. Ashraf, S. Gavenonis, D. Daye, C. Mies, M. Feldman, M. Rosen, and D. Kontos, "A multichannel Markov random field approach for automated segmentation of breast cancer tumor in DCE-MRI data using kinetic observation model," in *Proc. 14th Int. Conf. Med. Image Comput. Comput.-Assist. Intervent.*, Toronto, ON, Canada. Cham, Switzerland: Springer, Sep. 2011, pp. 546–553.

[28] F. H. Alghamedy, M. Shafiq, L. Liu, A. Yasin, R. A. Khan, and H. S. Mohammed, "Machine learning-based multimodel computing for medical imaging for classification and detection of Alzheimer disease," *Comput. Intell. Neurosci.*, vol. 2022, no. 1, Aug. 2022, Art. no. 9211477.

[29] M. Rahimpour, M.-J. Saint Martin, F. Frouin, P. Akl, F. Orlhac, M. Koole, and C. Malhaire, "Visual ensemble selection of deep convolutional neural networks for 3D segmentation of breast tumors on dynamic contrast enhanced MRI," *Eur. Radiol.*, vol. 33, no. 2, pp. 959–969, Sep. 2022.

[30] W. K. Cheung, R. Bell, A. Nair, L. J. Menezes, R. Patel, S. Wan, K. Chou, J. Chen, R. Torii, R. H. Davies, J. C. Moon, D. C. Alexander, and J. Jacob, "A computationally efficient approach to segmentation of the aorta and coronary arteries using deep learning," *IEEE Access*, vol. 9, pp. 108873–108888, 2021.

[31] W. K. Cheung, A. Pakzad, N. Mogulkoc, S. H. Needleman, B. Rangelov, E. Gudmundsson, A. Zhao, M. Abbas, D. McLaverty, D. Asimakopoulos, R. Chapman, R. Savas, S. M. Janes, Y. Hu, D. C. Alexander, J. R. Hurst, and J. Jacob, "Interpolation-split: A data-centric deep learning approach with big interpolated data to boost airway segmentation performance," *J. Big Data*, vol. 11, no. 1, p. 104, Aug. 2024, doi: 10.1186/s40537-024-00974-x.

[32] J. Dai, Y. Li, K. He, and J. Sun, "R-FCN: Object detection via region-based fully convolutional networks," in *Proc. Adv. Neural Inf. Process. Syst.*, Jan. 2016, pp. 1–12.

[33] O. Oktay, J. Schlemper, L. Le Folgoc, M. Lee, M. Heinrich, K. Misawa, K. Mori, S. McDonagh, N. Y. Hammerla, B. Kainz, B. Glocker, and D. Rueckert, "Attention U-Net: Learning where to look for the pancreas," 2018, *arXiv:1804.03999*.

[34] Z. Zhao, S. Du, Z. Xu, Z. Yin, X. Huang, X. Huang, C. Wong, Y. Liang, J. Shen, J. Wu, J. Qu, L. Zhang, Y. Cui, Y. Wang, L. Wee, A. Dekker, C. Han, Z. Liu, Z. Shi, and C. Liang, "SwinHR: Hemodynamic-powered hierarchical vision transformer for breast tumor segmentation," *Comput. Biol. Med.*, vol. 169, Feb. 2024, Art. no. 107939.

[35] J. Ru, B. Lu, B. Chen, J. Shi, G. Chen, M. Wang, Z. Pan, Y. Lin, Z. Gao, J. Zhou, X. Liu, and C. Zhang, "Attention guided neural ODE network for breast tumor segmentation in medical images," *Comput. Biol. Med.*, vol. 159, Jun. 2023, Art. no. 106884.

[36] Y. Liu, H. Liu, Z. Zhao, L. Zhang, and X. Liu, "A new active contour model-based segmentation approach for accurate extraction of the lesion from breast DCE-MRI," in *Proc. IEEE Int. Conf. Image Process.*, Sep. 2013, pp. 1140–1143.

[37] S. C. Agner, J. Xu, and A. Madabhushi, "Spectral embedding based active contour (SEAC) for lesion segmentation on breast dynamic contrast enhanced magnetic resonance imaging," *Med. Phys.*, vol. 40, no. 3, Mar. 2013, Art. no. 032305.

[38] B.-W. Hong, "Joint estimation of shape and deformation for the detection of lesions in dynamic contrast-enhanced breast MRI," *Phys. Med. Biol.*, vol. 58, no. 21, pp. 7757–7775, Nov. 2013.

[39] H. Liu, Y. Liu, Z. Zhao, L. Zhang, and T. Qiu, "A new background distribution-based active contour model for three-dimensional lesion segmentation in breast DCE-MRI," *Med. Phys.*, vol. 41, no. 8, Aug. 2014, Art. no. 082303.

[40] J. Yin, J. Yang, and Z. Jiang, "Classification of breast mass lesions on dynamic contrast-enhanced magnetic resonance imaging by a computer-assisted diagnosis system based on quantitative analysis," *Oncol. Lett.*, vol. 17, no. 3, pp. 2623–2630, Jan. 2019.

[41] O. Zavala-Romero, A. Meyer-Baese, and M. B. I. Lobbes, "Breast lesion segmentation software for DCE-MRI: An open source GPGPU based optimization," in *Proc. IEEE 15th Int. Symp. Biomed. Imag. (ISBI)*, Apr. 2018, pp. 211–215.

[42] H. Veeraraghavan, B. Z. Dashevsky, N. Onishi, M. Sadinski, E. Morris, J. O. Deasy, and E. J. Sutton, "Appearance constrained semi-automatic segmentation from DCE-MRI is reproducible and feasible for breast cancer radiomics: A feasibility study," *Sci. Rep.*, vol. 8, no. 1, p. 4838, Mar. 2018.

[43] P. Jaglan, R. Dass, and M. Duhan, "An automatic and efficient technique for tumor location identification and classification through breast MR images," *Expert Syst. Appl.*, vol. 185, Dec. 2021, Art. no. 115580.

[44] J. Zhang, A. Saha, Z. Zhu, and M. A. Mazurowski, "Hierarchical convolutional neural networks for segmentation of breast tumors in MRI with application to radiogenomics," *IEEE Trans. Med. Imag.*, vol. 38, no. 2, pp. 435–447, Feb. 2019.

[45] M. Qiao, S. Suo, F. Cheng, J. Hua, D. Xue, Y. Guo, J. Xu, and Y. Wang, "Three-dimensional breast tumor segmentation on DCE-MRI with a multilabel attention-guided joint-phase-learning network," *Computerized Med. Imag. Graph.*, vol. 90, Jun. 2021, Art. no. 101909.

[46] H. Wang, J. Cao, J. Feng, Y. Xie, D. Yang, and B. Chen, "Mixed 2D and 3D convolutional network with multi-scale context for lesion segmentation in breast DCE-MRI," *Biomed. Signal Process. Control*, vol. 68, Jul. 2021, Art. no. 102607.

[47] E. Kim, H.-H. Cho, J. Kwon, Y.-T. Oh, E. S. Ko, and H. Park, "Tumor-attentive segmentation-guided GAN for synthesizing breast contrast-enhanced MRI without contrast agents," *IEEE J. Transl. Eng. Health Med.*, vol. 11, pp. 32–43, 2022.

[48] C. Qin, Y. Wu, J. Zeng, L. Tian, Y. Zhai, F. Li, and X. Zhang, "Joint transformer and multi-scale CNN for DCE-MRI breast cancer segmentation," *Soft Comput.*, vol. 26, no. 17, pp. 8317–8334, Sep. 2022.

[49] T. Lv, Y. Wu, Y. Wang, Y. Liu, L. Li, C. Deng, and X. Pan, "A hybrid hemodynamic knowledge-powered and feature reconstruction-guided scheme for breast cancer segmentation based on DCE-MRI," *Med. Image Anal.*, vol. 82, Nov. 2022, Art. no. 102572.

[50] S. Wang, K. Sun, L. Wang, L. Qu, F. Yan, Q. Wang, and D. Shen, "Breast tumor segmentation in DCE-MRI with tumor sensitive synthesis," *IEEE Trans. Neural Netw. Learn. Syst.*, vol. 34, no. 8, pp. 4990–5001, Aug. 2021.

[51] L. Wang, L. Wang, Z. Kuai, L. Tang, Y. Ou, M. Wu, T. Shi, C. Ye, and Y. Zhu, "Progressive dual priori network for generalized breast tumor segmentation," *IEEE J. Biomed. Health Informat.*, vol. 28, no. 9, pp. 5459–5472, Sep. 2024.

[52] L. Zhou, Y. Zhang, J. Zhang, X. Qian, C. Gong, K. Sun, Z. Ding, X. Wang, Z. Li, Z. Liu, and D. Shen, "Prototype learning guided hybrid network for breast tumor segmentation in DCE-MRI," *IEEE Trans. Med. Imag.*, vol. 44, no. 1, pp. 244–258, Jan. 2025.

[53] A. Akbar, S. Han, N. U. Rehman, R. Irshad, K. Ahmed, M. M. Ali, and A. A. Mazroa, "Reinforcement tokenization and graph convolution for high-precision breast tumor segmentation in DCE-MRI," *Biomed. Signal Process. Control*, vol. 100, Feb. 2025, Art. no. 106947.

[54] C. Sahaya Pushpa Sarmila Star, T. M. Inbamalar, and A. Milton, "Automatic semantic segmentation of breast cancer in DCE-MRI using DeepLabV3+ with modified ResNet50," *Biomed. Signal Process. Control*, vol. 99, Jan. 2025, Art. no. 106691.

[55] M. Shafiq, Q. Fan, F. H. Alghamedy, and W. J. Obidallah, "DualEye-FeatureNet: A dual-stream feature transfer framework for multi-modal ophthalmic image classification," *IEEE Access*, vol. 12, pp. 143985–144008, 2024.

[56] A. Bilal, X. Liu, T. I. Baig, H. Long, and M. Shafiq, "EdgeSVDNet: 5G-enabled detection and classification of vision-threatening diabetic retinopathy in retinal fundus images," *Electronics*, vol. 12, no. 19, p. 4094, Sep. 2023.

[57] A. Ruszczynski, *Nonlinear Optimization*. Princeton, NJ, USA: Princeton Univ. Press, 2011.

[58] J. L. Troutman, *Variational Calculus With Elementary Convexity*. Cham, Switzerland: Springer, 2012.

[59] R. Fletcher, *Practical Methods of Optimization*. Hoboken, NJ, USA: Wiley, 2000.

[60] A. Saha, M. R. Harowicz, L. J. Grimm, J. Weng, E. Cain, C. Kim, S. Ghate, R. Walsh, and M. A. Mazurowski, 2021, "Dynamic contrast-enhanced magnetic resonance images of breast cancer patients with tumor locations," *The Cancer Imaging Archive*.

[61] W. Huang et al., "Variations of dynamic contrast-enhanced magnetic resonance imaging in evaluation of breast cancer therapy response: A multicenter data analysis challenge," *Transl. Oncol.*, vol. 7, no. 1, pp. 153–166, Feb. 2014.

[62] W. Lingle, B. Erickson, M. Zuley, R. Jarosz, E. Bonaccio, J. Filippini, J. Net, L. Levi, E. Morris, G. Figler, P. Elnajjar, S. Kirk, Y. Lee, M. Giger, and N. Gruszauskas, 2016, "The cancer genome atlas breast invasive carcinoma collection (TCGA-BRCA)," *The cancer imaging archive*.

[63] X. Zhao, Y. Liao, J. Xie, X. He, S. Zhang, G. Wang, J. Fang, H. Lu, and J. Yu, "BreastDM: A DCE-MRI dataset for breast tumor image segmentation and classification," *Comput. Biol. Med.*, vol. 164, Sep. 2023, Art. no. 107255.

[64] C. Meyer, T. Chenevert, C. Galbán, T. Johnson, D. Hamstra, A. Rehemtulla, and B. Ross, 2015, "Rider breast MRI, *The cancer imaging archive*.

[65] D. Newitt and N. Hylton, "Multi-center breast DCE-MRI data and segmentations from patients in the I-SPY 1/ACRIN 6657 trials," *Cancer Imag. Arch.*, vol. 10, no. 7, pp. 1–12, 2016.

[66] D. P. Huttenlocher, G. A. Klanderman, and W. J. Rucklidge, "Comparing images using the Hausdorff distance," *IEEE Trans. Pattern Anal. Mach. Intell.*, vol. 15, no. 9, pp. 850–863, Sep. 1993.

[67] N. U. Rehman, J. Wang, H. Weiyan, I. Ali, A. Akbar, M. Assam, Y. Y. Ghadi, and A. Algarni, "Edge of discovery: Enhancing breast tumor MRI analysis with boundary-driven deep learning," *Biomed. Signal Process. Control*, vol. 95, Sep. 2024, Art. no. 106291.

[68] R. Khaled, J. Vidal, J. C. Vilanova, and R. Martí, "A U-Net ensemble for breast lesion segmentation in DCE MRI," *Comput. Biol. Med.*, vol. 140, Jan. 2022, Art. no. 105093.

[69] Ö. Çiçek, A. Abdulkadir, S. S. Lienkamp, T. Brox, and O. Ronneberger, "3D U-Net: Learning dense volumetric segmentation from sparse annotation," in *Proc. 19th Int. Conf. Med. Image Comput. Comput.-Assist. Intervent.*, Athens, Greece. Cham, Switzerland: Springer, Oct. 2016, pp. 424–432.

[70] F. Milletari, N. Navab, and S.-A. Ahmadi, "V-net: Fully convolutional neural networks for volumetric medical image segmentation," in *Proc. 4th Int. Conf. 3D Vis. (3DV)*, Oct. 2016, pp. 565–571.

[71] A. Hatamizadeh, Y. Tang, V. Nath, D. Yang, A. Myronenko, B. Landman, H. R. Roth, and D. Xu, "UNETR: Transformers for 3D medical image segmentation," in *Proc. IEEE/CVF Winter Conf. Appl. Comput. Vis. (WACV)*, Jan. 2022, pp. 1748–1758.

[72] F. Isensee, P. F. Jaeger, S. A. A. Kohl, J. Petersen, and K. H. Maier-Hein, "NnU-Net: A self-configuring method for deep learning-based biomedical image segmentation," *Nature Methods*, vol. 18, no. 2, pp. 203–211, Feb. 2021.

[73] J. Long, E. Shelhamer, and T. Darrell, "Fully convolutional networks for semantic segmentation," in *Proc. IEEE Conf. Comput. Vis. Pattern Recognit. (CVPR)*, Jun. 2015, pp. 3431–3440.

[74] L.-C. Chen, G. Papandreou, I. Kokkinos, K. Murphy, and A. L. Yuille, "DeepLab: Semantic image segmentation with deep convolutional nets, atrous convolution, and fully connected CRFs," *IEEE Trans. Pattern Anal. Mach. Intell.*, vol. 40, no. 4, pp. 834–848, Apr. 2018.

[75] H. Zhao, J. Shi, X. Qi, X. Wang, and J. Jia, "Pyramid scene parsing network," in *Proc. IEEE Conf. Comput. Vis. Pattern Recognit. (CVPR)*, Jul. 2017, pp. 6230–6239.

[76] J. M. J. Valanarasu, P. Oza, I. Hacihaliloglu, and V. M. Patel, "Medical transformer: Gated axial-attention for medical image segmentation," in *Proc. 24th Int. Conf. Med. Image Comput. Comput. Assist. Intervent.*, Strasbourg, France. Cham, Switzerland: Springer, Oct. 2021, pp. 36–46.

[77] T. Duc Bui, J. Shin, and T. Moon, "3D densely convolutional networks for volumetric segmentation," 2017, *arXiv:1709.03199*.

PRIYADHARSHINI BABU is currently pursuing the Ph.D. degree in tumor segmentation, analysis, and treatment response in breast cancer. She is a Research Scholar under the supervision of Dr. Mythili Asaithambi, a Professor with the Sensor and Biomedical Technology Division, School of Electronics Engineering, Vellore Institute of Technology, Vellore, India.

MYTHILI ASAITHAMBI (Member, IEEE) received the Ph.D. degree from Madras Institute of Technology, Anna University. She also availed DST-PURSE Fellowship during the Ph.D. degree. She is currently a Professor with the Sensor and Biomedical Technology Division, School of Electronics Engineering, Vellore Institute of Technology, Vellore, India. She has published more than 30 papers in journals and conferences. Her current research interest includes medical image processing with machine learning.

SUDHAKAR MOGAPPAIR SURIYAKUMAR is currently an Associate Professor with the School of Electronics Engineering, Vellore Institute of Technology, Vellore, India. He has several years of industrial and research and development experience in tier-1 organizations. He has authored or co-authored a sufficient number of research articles in Science Citation Index journals and is also the PI for a research project with Indian Space Research Organization (ISRO). His research interests include machine learning and its applications, such as computer vision, data mining, image processing, information retrieval, and pattern recognition.

● ● ●